NUREG-0264-2

SUPPRESSION POOL DYNAMICS

Quarterly Progress Report
October 1, 1976 - December 31, 1976

University of California at Los Angeles
for
U. S. Nuclear Regulatory Commission

Available from
National Technical Information Service
Springfield, Virginia 22161
Price: Printed Copy $5.00 ; Microfiche $3.00

NUREG-0264-2
NRC-2,4

SUPPRESSION POOL DYNAMICS

Quarterly Progress Report
October 1, 1976 - December 31, 1976

I. Catton
C. K. Chan
H. H. Chiou
J. D. Weaver
V. K. Dhir
C. K. B. Lee
C. Y. Tsui

Manuscript Completed: January 1977
Date Published: May 1977

School of Engineering and Applied Science
University of California
Los Angeles, CA 90024

Prepared for
Division of Reactor Safety Research
Office of Nuclear Regulatory Research
U. S. Nuclear Regulatory Commission
Under Contract No. AT(48-24)-342

NOTICE

This report was prepared as an account of work sponsored by the United States Government. Neither the United States nor the United States Nuclear Regulatory Commission, nor any of their employees nor the University of California or its employees, makes any warranty, express or implied, or assumes any legal liability or responsibility for the accuracy, completeness or usefulness of any information, apparatus, product or process disclosed, or represents that its use would not infringe privately owned rights.

SUMMARY

This report presents the results of transient air-water tests conducted between October 1 to December 31, 1976, to investigate basic hydrodynamical phenomena that can be experienced in a BWR Pressure Suppression Pool at the onset of a Loss of Coolant Accident. Based on the observation of the Taylor instability the scaling of vent clearing phenomena was reconsidered. The governing similitude parameters are found to be the Froude number gL/U^2, the Euler number $P_c/\rho_c U^2$ and the Weber number $\rho_c LU^2/\sigma$.

The tests were performed in a cylindrical plexiglass test chamber. Air was injected downward through pipes of different diameters placed in the middle of the test chamber containing water at room temperature.

The inflow of the air is observed to form a depression on the liquid surface. As the liquid is accelerated and pushed into the water pool, the Taylor instability breaks up the interface and a water spike is seen to grow into the gaseous region, but it is broken up prior to complete vent clearing. The break-up creates a two phase region behind the primary interface. The liquid spike grows monotonically with time but the growth rate slows down as the liquid spike attains a finite height. The velocity and the acceleration of the liquid-gas interface increases rapidly with time during the early stages of vent clearing but the interface slows down considerably during the later periods. The growth of the water spike is found to be extremely non-linear.

Based on these experimental observations, the liquid slug model for vent clearing was modified to take into account the effect of reduced liquid acceleration. If the liquid left in the pipe at the time of the vent clearing was considered in the model, it was found that the modified

theory did predict well the vent clearing phenomena.

The results of our bench-type experiments were applied to the case of a BWR pressure suppression pool. Though the maximum acceleration experienced by the liquid column in the prototype is less than observed in the laboratory experiments, yet it is about six times greater in magnitude than earth normal gravity (g). The instabilities at the interface are expected to grow when the acceleration reaches 0.1 g, which corresponds to the shortest wavelength that can be accommodated in the vent. Because of the non-linear characteristics of the instability, the interfacial behavior of the prototype is much more complicated.

After vent clearing, the bubble is observed to grow spherically only for a very short period of time and soon the bubble shape is controlled by a balance between gravity and intertia forces. The inertia forces tend to elongate the bubble while the buoyancy tends to flatten it. Higher upstream pressure increases the intertia of the airstream whereas greater submergence depths enhance the buoyancy effects. The final size of the bubble prior to detachment and the time taken by the bubble to reach the final size are also dependent on the upstream pressure and the submergence depth. The final size of the bubble in turn controls the free surface response.

The similitude analysis for steam condensation indicates that the governing parameters are the Fourier number, the Froude number, the Specific Heat Ratio, the Euler number and the Mach number. Preliminary data for forces at the bottom of the pool have also been obtained.

TABLE OF CONTENTS

LIST OF FIGURES

LIST OF FIGURES (Continued)

LIST OF TABLES

LIST OF SYMBOLS

A	Area
C_p	Heat capacity
d	Diameter
Eu	Euler number
Fo	Fourier number
f	Fanno Friction
g	Gravitational constant
h_{fg}	Latent heat of evaporation
k	Thermal conductivity
L	Length
M	Mach number
m	Mass
$\dot{m}$	Condensation rate
P	Pressure
P_o	Dry well
P_s	Suppression pool pressure
P_1	Air-water interface
P_2	Water spike height
R	Principal radii
$\dot{\vec{r}}$	Interfacial velocity
T	Temperature
t	Time
U	Characteristic velocity
u	Velocity
W	Growth rate

We	Weber number
X	Co-ordinate
α	Thermal diffusivity
η	Interface co-ordinate
λ	Wavelength
ρ	Density
σ	Surface tension
ϕ	Velocity potential

Subscripts

c	Characteristic
i	Interface
ℓ	Liquid
v	Vapor
w	Water

1. INTRODUCTION

This is the second quarterly report of an experimental program conducted at UCLA to investigate related thermal and hydraulic phenomena that might affect the structural integrity of the Pressure Suppression Pool in the event of a LOCA. The program emphasizes fundamental understanding of the physical processes that control the BWR system behavior.

During the first quarter, a research team was assembled and the experimental apparatus for transient air injection into an axisymmetric chamber was designed and fabricated. Data for vent clearing phenomena were obtained. Scaling for transient air injection was also established. From the motion pictures of the vent clearing process, it was observed that a considerable mass of liquid was held in the tube during the injection of the liquid slug as a result of surface instability. The results of our first quarter effort have been presented in our first quarterly report.

During the second quarter, further study probed into the surface instability problem. More refinements of the apparatus and instrumentation were completed. Data for pressure forces generated on the bottom of the pool during vent clearing and data for bubble formation were obtained. Preliminary design of the single vent steam injector was completed. Because of the delay in the delivery of the steam boiler, the experiment is not expected to be started until April 1977. However, a preliminary study of the scaling law for steam injection was completed.

For the next quarter, more data will be obtained for the pressure force and the swelling height. A portion of the steam jet apparatus will be fabricated and instrumentation will be tested.

2. SCALING AND ANALYSIS

2.1. Further Consideration of Scaling Laws in Vent Clearing

It has been observed in the vent clearing experiment that the air-liquid interface was disturbed as a result of a Taylor instability. Liquid was observed to be left behind on the wall in the form of a film as a result of the viscous effect. The experimental results show that the growth of the instability is linear for a very short time. The liquid surface rapidly changes to a liquid spike moving into the gaseous region. Based on this observation, the transient motion of the water slug in the vent during the vent clearing transient cannot be treated as for a rigid body. Both the Taylor instability and the viscous effect tend to reduce the effective mass of the accelerating column of liquid and hence the actual vent clearing time is less than that predicted by the rigid body slug equation,

$$\frac{d(mu)}{dt} + \rho_w u^2 A = [(P_o - P_s) - \rho_w x]A - \frac{f_m(L - x)u^2 A}{2d} \qquad (2.1)$$

The details of this equation have been discussed in our first quarterly report. In order to incorporate the instability effect into the vent clearing model, two approaches were adopted. In the first one, scaling laws in vent clearing were reconsidered and new parameters were defined. In the second approach, the effective mass of the accelerating liquid column was adjusted to accomodate the instability "left-over."

Because of the surface instability, Equation (2.1) cannot be considered as the sole governing equation for the vent clearing phase. The equation that governs the surface instability has to be considered. By introducing the velocity potential ϕ such that

$$\phi = \vec{\nabla} \cdot \vec{u} \qquad (2.2)$$

The momentum equation for the interface can be written

$$\frac{\partial \phi}{\partial t} + \frac{1}{2} \nabla\phi \cdot \nabla\phi + a\eta = \frac{P}{\rho_w} + \frac{\sigma}{\rho_w} \left\{ \nabla \cdot \left[\frac{\nabla \eta}{(1 + \nabla\eta \cdot \nabla\eta)^{1/2}} \right] \right\} \tag{2.3}$$

where

P = applied pressure

ρ_w = liquid density

η = interfacial position relative to x where x is the base of the water spike. It is related to the slug velocity u by

$dx/dt = u$

a = net acceleration, i. e. true acceleration minus the gravity, and

σ = surface tension

We introduce the following quantities as characteristic variables:

L = characteristic length

ρ_c = characteristic density

U = characteristic velocity

P_c = characteristic pressure

g_c = characteristic acceleration

t_c = characteristic time.

Neglecting the frictional effect in Equation (1.1), two dimensionless groups that appear in that equation are: the Froude number, $Fr = gL/U^2$, and the Euler number, $Eu = P_c/(\rho_c U^2)$. In non-dimensioning Equation (2.2), besides the Froude and Euler numbers, there is the additional group Weber number, $We = \rho_c L U^2/\sigma$. Similitude requires that

$$\left(\frac{gL}{U^2}\right)_p = \left(\frac{gL}{U^2}\right)_m \tag{2.4}$$

$$\left(\frac{P_c}{\rho_c U^2}\right)_p = \left(\frac{P_c}{\rho_c U^2}\right)_m \tag{2.5}$$

$$\left(\frac{\rho_c L U^2}{\sigma}\right)_p = \left(\frac{\rho_c L U^2}{\sigma}\right)_m . \tag{2.6}$$

Subscripts p and m represent quantities for the prototype and the model respectively. Similitude in the Froude number leads to the required scaling of the characteristic velocities,

$$U_p/U_m = \sqrt{L_p/L_m} . \tag{2.7}$$

The scaling of pressure is

$$\frac{(P_c/\rho_c)_p}{(P_c/\rho_c)_m} = \frac{L_p}{L_m} \qquad \text{or} \qquad \frac{P_{cp}}{P_{cm}} \frac{\rho_{cm}}{\rho_{cp}} = \frac{L_p}{L_m}. \tag{2.8}$$

The scaling of density and surface tension had to be

$$\frac{(\rho_c/\sigma)_p}{(\rho_c/\sigma)_m} = \left(\frac{L_m}{L_p}\right)^3. \tag{2.9}$$

Hence, assuming a 1/12 scale experiment, we find that the simulation would not be realistic if the working medium is water. In order to simulate the instability, a working fluid must be chosen in such a way that its properties in relation to the water properties in the prototype satisfy Equation (2.9). That means the liquid in the model has to be heavier but with less surface tension. For 1/12 scale, this might impose some practical problems. Actually, the Weber number based on the system length is probably only important in the initial stage of the spike formation. During the growth stage the characteristic length would be the wavelength.

2.2. Further Consideration of the Theoretical Model for Vent Clearing

The interface between the air and the water in the vent pipe was observed to be broken up into two distinct regions as shown in Figures 2.1 and 2.2. The first region is the bubble formed in the early stage

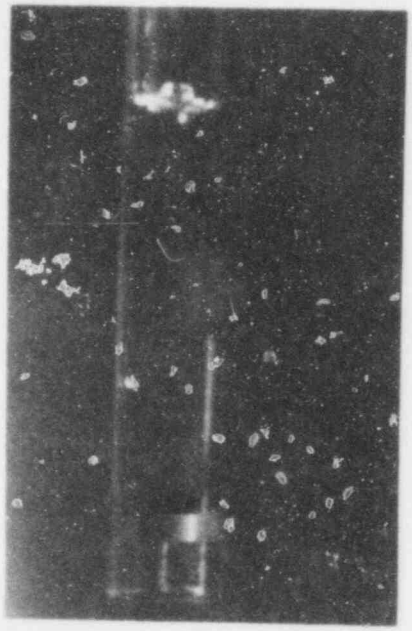

t = .040 sec

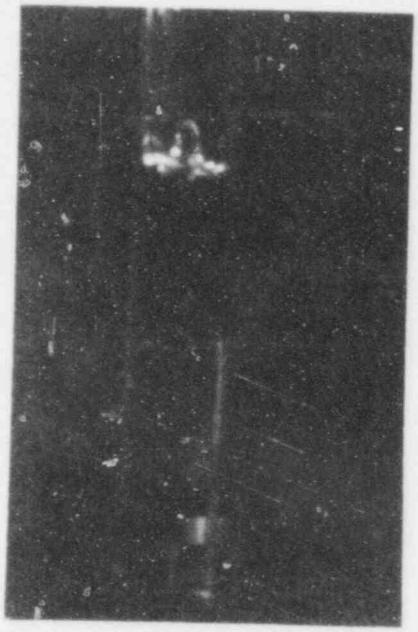

t = .045 sec

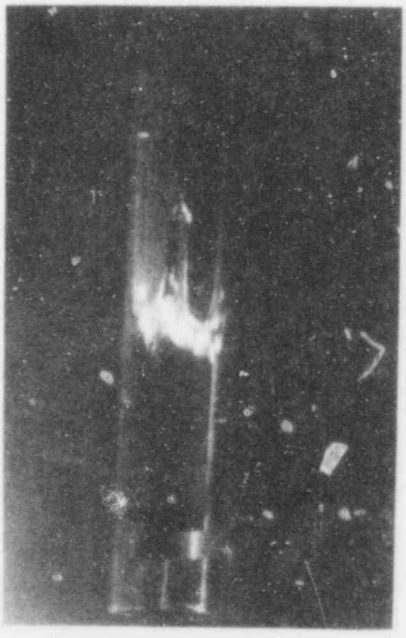

t = .066 sec

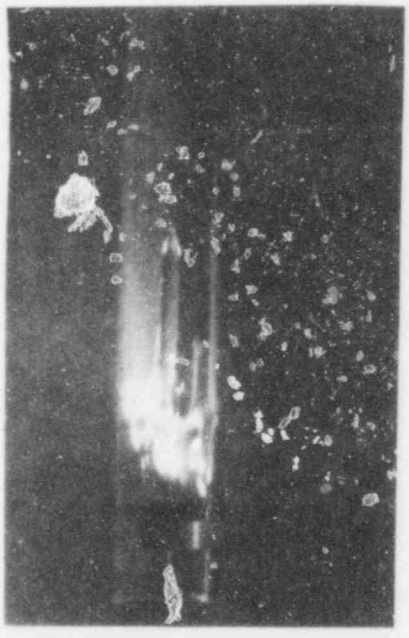

t = .072 sec

Fig. 2.1. Sequence of interface formation during vent clearing.
Interface movement starts at t = 0 sec.
Upstream pressure = 122 κPa.
Tube diameter (I.D.) = 4.6 cm.

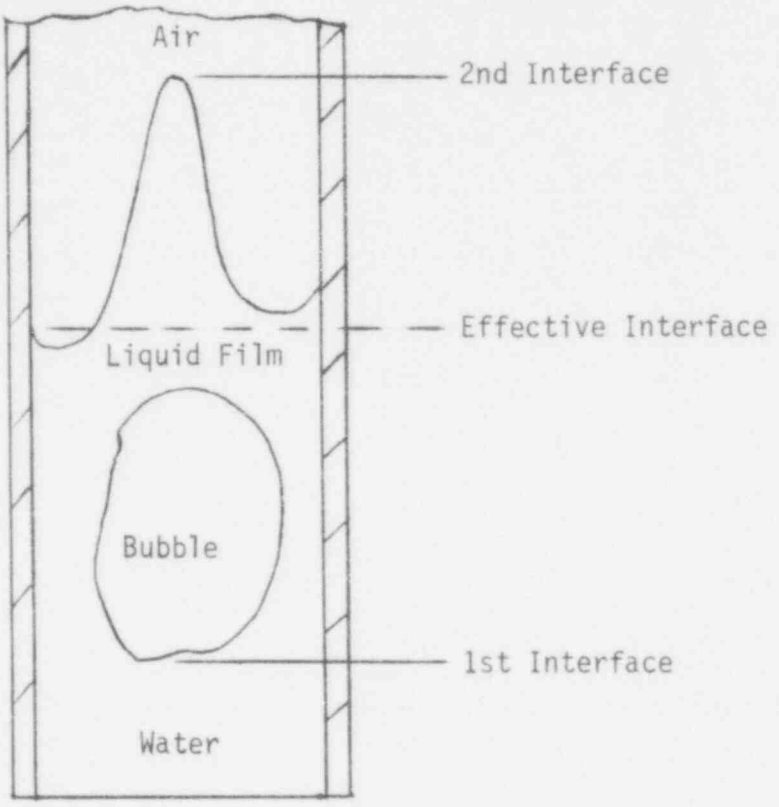

Figure 2.2.

Interfacial Behavior in Vent Clearing.

of the vent clearing. The second region is the water film between the bubble and the air stream. The three interfaces bounding these two regions are defined in Figure 2.1. In order to incorporate the phenomena with the solid body motion equation (Equation (2.1)), an effective interface has to be defined. The location of this effective interface is taken as the point at which the air and the water would have been separated as if there were no instability. It is observed that when the first interface clears at the pipe exit, the bubble tends to slow down the velocity of the water film which separates the bubble from the air column in such a way that there is a delay time for vent clearing of the second and third interfaces as shown in Figure 2.2.

Since the formation of the bubble is a rather random process, an exact analysis is not attempted at this point. A semi-empirical approach is adopted to investigate the adequacy of the water slug model. The water volume left in the pipe at the time of the vent clearing of the first interface is first determined. An effective interface location is calculated based on the water volume. The time predicted from the theory for the interface to arrive at the effective location is then compared with the measured time of the first interface vent clearing. Two cases were considered and their results are shown in Table 2.1. It can be seen that the theory did predict well the vent clearing time if the effective interface concept was utilized. In other words, the vent clearing model without the incorporation of the instability effects would probably overpredict the vent clearing time.

2.3. Scaling Laws for Steam Jet Condensation

In designing a scale model to study the steam jet phenomenon in

	Case 1	Case 2
Submergence Depth (cm)	30	30
Pipe Inner Diameter (cm)	4.7	4.7
Tank Pressure (kPa)	122	163
Water Volume at First Interface (cm^3)	43.57	24.83
Vent Clearing Effective Interface Location (cm)	27.49	1.43
Measured Vent Clearing Time (sec)	0.09118	0.08701
Predicted Vent Clearing Time (sec)	0.09148	0.0825
Percent Difference between Predicted and Measured Values	0.32	5.3

Table 2.1.

Comparison of Predicted and Measured Vent Clearing Times.

729 071

subcooled water, it is important to preserve the prominent parameters of the prototype, so it can guarantee that all governing effects are included and that negligible effects are excluded. For the transient steam jet in a subcooled liquid, the governing equations for the incompressible liquid medium are

$$\nabla \cdot \vec{u}_\ell = 0 \tag{2.10}$$

$$\frac{D\vec{u}_\ell}{Dt} = -\frac{1}{\rho_\ell} \nabla P_\ell \tag{2.11}$$

$$\frac{DT_\ell}{Dt} = \alpha_\ell \nabla^2 T_\ell \tag{2.12}$$

where

$\vec{u}_\ell$ = liquid velocity vector

P_ℓ = liquid pressure

ρ_ℓ = liquid density

T_ℓ = liquid temperature

α_ℓ = liquid thermal diffusivity.

For the vapor region, the governing equations are

$$\frac{\partial \rho_v}{\partial t} + \nabla \cdot \rho_v \vec{u}_v = 0 \tag{2.13}$$

$$\frac{D\vec{u}_v}{Dt} = -\frac{1}{\rho_v} \nabla P_v \tag{2.14}$$

$$\frac{DT_v}{Dt} = \alpha_v \nabla^2 T_v + \frac{1}{\rho_v C_{pv}} \frac{DP_v}{Dt}. \tag{2.15}$$

where

$\vec{u}_v$ = vapor velocity vector

P_v = vapor pressure

ρ_v = vapor density

T_v = vapor temperature

α_v = vapor thermal diffusivity

C_{pv} = vapor thermal capacity.

At the interface, $\vec{r}_i$, the conservation of mass, momentum and energy requires that

$$\rho_v(\vec{u}_v - \dot{\vec{r}}_i)\cdot\hat{n} = \rho_\ell(\vec{u}_\ell - \dot{\vec{r}}_i)\cdot\hat{n} = \dot{m} \tag{2.16}$$

$$P_v - P_\ell = \sigma\left(\frac{1}{R_1} + \frac{1}{R_2}\right) \tag{2.17}$$

$$k_\ell \frac{\partial T_\ell}{\partial \eta} - k_v \frac{\partial T_v}{\partial \eta} = \dot{m} h_{fg} \tag{2.18}$$

where

$\dot{\vec{r}}_i$ = interfacial velocity

$\hat{n}$ = normal vector at the interface

$\dot{m}$ = condensation rate

σ = surface tension

R_1, R_2 = principal radii

h_{fg} = heat of evaporation

In Equation (2.17), liquid viscosity effect and momentum transfer due to steam condensation are neglected and the viscous dissipation and kinetic energy have not been included. If equilibrium is assumed at the interface, then

$$T_{v_i} = T_{\ell_i} \tag{2.19}$$

and the pressure is approximated from the Clausius-Clapeyron relation

$$P_{v_i} = P_{v_o} \exp\left[\frac{h_{fg}}{R_g T_{i_o}}\left(1 - \frac{T_{i_o}}{T_i}\right)\right] \tag{2.20}$$

where

T_{v_i} = vapor temperature at the interface,

T_{ℓ_i} = liquid temperature at the interface

P_{v_i} = vapor pressure at the interface

P_{v_o} = reference vapor pressure

T_{i_o} = reference vapor temperature.

If r_c = characteristic length,

U_c = characteristic velocity

t_c = characteristic time = r_c/U_c

P_c = characteristic pressure

ρ_c = characteristic density

T_c = characteristic temperature

α_c = characteristic thermal diffusivity

C_{pc} = characteristic thermal capacity

h_c = characteristic enthalpy = $C_{pc}T_c$.

Equations (2.10) to (2.18) can be expressed in non-dimensional form as

$$\nabla \cdot \vec{U}^*_\ell = 0 \tag{2.21}$$

$$\frac{D\vec{u}^*_\ell}{Dt^*} = - Eu \frac{1}{\rho^*_\ell} \nabla P^*_\ell \tag{2.22}$$

$$\frac{DT^*_\ell}{Dt^*} = Fo\ \alpha^*_\ell \nabla^2 T^*_\rho \tag{2.23}$$

$$\frac{\partial \rho^*_v}{\partial t^*} + \nabla \cdot \rho^*_v \vec{u}^*_v = 0 \tag{2.24}$$

$$\frac{D\vec{u}^*_v}{Dt^*} = - Eu \frac{1}{\rho^*_c} \nabla P^*_v \tag{2.25}$$

$$\frac{DT_v^*}{Dt^*} = Fo\ \alpha_v^* \nabla^2 T_v^* + \frac{Eu\ M^2}{(\gamma - 1)} \frac{1}{\rho_v^* C_{pv}^*} \frac{DP_v^*}{Dt^*} \tag{2.26}$$

$$\rho_v^*(\vec{u}_v^* - \dot{\vec{r}}^*) \cdot \hat{n}^* = \rho_\ell^*(\vec{u}^* - \dot{\vec{r}}^*) \cdot \hat{n}^* = \dot{m}^* \tag{2.27}$$

$$P_v^* - P_\ell^* = \frac{1}{Eu\ We} \left(\frac{1}{R_1^*} + \frac{1}{R_2^*}\right) \tag{2.28}$$

$$k_\ell^* \frac{\partial T_\ell^*}{\partial n^*} - k_v^* \frac{\partial T_v^*}{\partial n^*} = \frac{1}{Fo} \dot{m}^* h_{fg}^* \tag{2.29}$$

$$T_{v_i}^* = T_{\ell_i}^* \tag{2.30}$$

$$P_v^* = P_{v_o}^* \exp\left[\frac{\gamma}{\gamma - 1} \frac{h_{fg}^*}{T_{i_o}^*} \left(1 - \frac{T_{i_o}^*}{T_i^*}\right)\right] \tag{2.31}$$

Hence the non-dimensionless groups are:

$$Fo = \text{the Fourier number} = \frac{\alpha_c t_c}{r_c^2} \tag{2.32}$$

$$\gamma = \text{the Specific Heat Ratio} = C_{pc}/C_{vc} \tag{2.33}$$

$$M = \text{the Mach number} = \left(\frac{U_c^2}{\gamma RT}\right)^{1/2} \tag{2.34}$$

$$We = \text{the Weber number} = \frac{\rho_c U_c^2 r_c}{\sigma}, \text{ and} \tag{2.35}$$

$$Eu = \text{the Euler number} = \frac{P_c}{\rho_c U_c^2}. \tag{2.36}$$

Hence if the working fluid for both the prototype and the model is the same for simulation of steam condensation in subcooled water, the velocity ratio is required to be

$$\frac{(U_c)_m}{(U_c)_p} = \frac{(r_c)_p}{(r_c)_m}, \tag{2.37}$$

the temperature ratio is required to be

$$\frac{(C_{pc}T_c)_m}{(C_{pc}T_c)_p} = \left[\frac{(r_c)_p}{(r_c)_m}\right]^2 \tag{2.38}$$

and the pressure ratio is required to be

$$\frac{(P_c/\rho_c)_m}{(P_c/\rho_c)_p} = \left[\frac{(r_c)_p}{(r_c)_m}\right]^2 \tag{2.39}$$

It should be noted that it is difficult to satisfy both the Fourier number and the Weber number at the same time if the working fluid for both the prototype and the model is water. Even if we can relax the Weber number, it is uncertain at this stage whether the simulation can be completely achieved in practice. However, some of the requirements can be relaxed depending on the physical situations. For example, at the end of the LOCA, the transient steam flow rate is slow so the Mach number effect can be ignored. Further study of the similitude laws and their application to the BWR LOCA transient will be continued.

2.4. Simulation for Stripping Phenomenon

Besides the governing equation for the steam condensation, the liquid surface experiences tangential viscious shear from a parallel gas stream. The equation predicts instability for a flat liquid surface and a parallel gas flow when

$$u^2 = \frac{1}{\alpha_1\alpha_2}\sqrt{\frac{\sigma g(\alpha_1 - \alpha_2)}{\rho_L + \rho_v}} \tag{2.40}$$

where

$$\alpha_1 = \frac{\rho_L}{\rho_L + \rho_v}$$

and

$$\alpha_2 = \frac{\rho_v}{\rho_L + \rho_v}.$$

If $\rho_L >> \rho_v$, $\alpha_1 = 1$ and $\alpha_2 = \rho_v/\rho_L$, then

$$u^2 = \frac{\rho_L}{\rho_v}\sqrt{\frac{\sigma g}{\rho_L}} \tag{2.41}$$

If the velocity near the surface is related to the exit velocity V_E by

$$u = V_E\left(\frac{d}{X}\right) \tag{2.42}$$

where

d = the diameter of the pipe, and

X = the distance from the jet,

then the similarity parameter for the stripping phenomenon is the Kelvin-Helmholtz instability number defined as

$$I_{K\text{-}H} = \frac{V_E^2 d^2}{X^2\left(\frac{\rho_L}{\rho_v}\sqrt{\frac{\sigma g}{\rho_L}}\right)} \tag{2.43}$$

Hence an additional similitude parameter

$$\frac{U_c^2}{\sqrt{\frac{\sigma g}{\rho_c}}} \tag{2.42}$$

should be included. The importance of this parameter also depends on the physical situation. It is less important for the air transient but becomes very important in the steam condensation process.

729 077

3. EXPERIMENTS

3.1. Role of Taylor Instability During Vent Clearing

During the vent clearing process, the liquid-gas interface is pushed out of the vent with an acceleration. The reaction of this acceleration is directed in a direction opposite to the gravitational force. The liquid-gas interface will remain stable as long as the magnitude of the reactive force is less than the gravitational force, because the net force would be directed from lighter to heavier fluid. However, the interface would become unstable when the acceleration force exceeds the gravitational force. Any perturbations at the interface would start to grow when the net acceleration directed from liquid to gas is such that the wavelength of the neutral wave is less than the diameter of the vent.

For incompressible, inviscid fluids of infinite depth, linearized instability theory gives [2] the minimum unstable wavelength as

$$\lambda_c = 2\pi\sqrt{\sigma/[a(\rho_w - \rho_a)]}, \tag{3.1}$$

the "fastest-growing" wavelength as

$$\lambda_d = 2\pi\sqrt{3}\,\sqrt{\sigma/[a(\rho_w - \rho_a)]} \tag{3.2}$$

and the growth rate of the "fastest-growing" wavelength as

$$w = 0.62\sqrt[4]{\frac{(\rho_w - \rho_a)^2 a^3}{\sigma(\rho_w + \rho_a)}}\,. \tag{3.3}$$

Visual observations made during the vent clearing phase of the experiments (46 mm tube) showed that the moving liquid interface indeed became unstable and a spike of liquid was seen standing on the interface. The spike of liquid was seen to grow with time but invariably broke up prior to complete clearing of the vent. Figures 3.1, 3.2 and 3.3 show

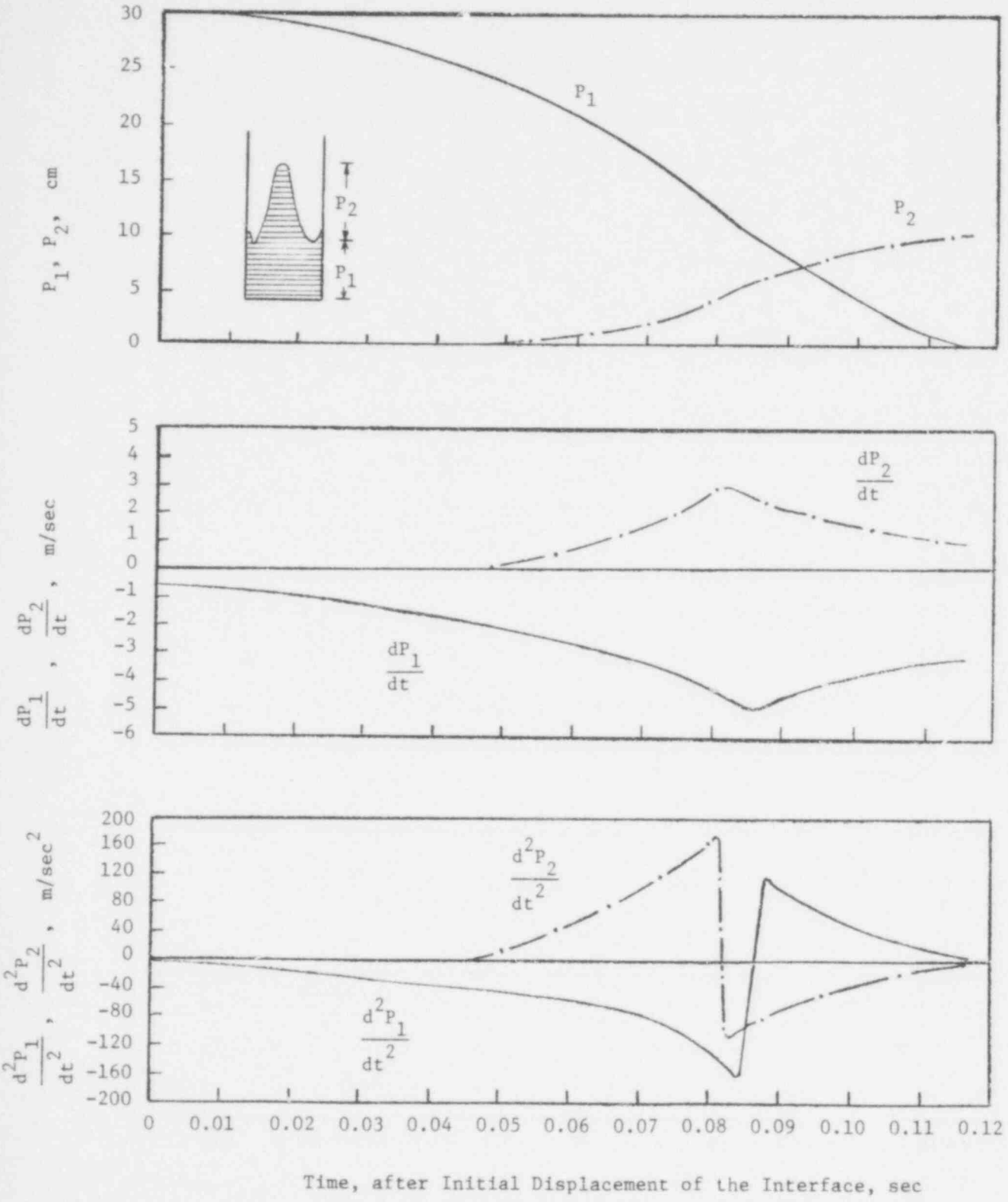

Fig. 3.1. Position, Velocity and Acceleration of the Air-Water Interfaces during Vent Clearing (46 mm ID Tube) with Upstream Pressure of 115.1 kPa.

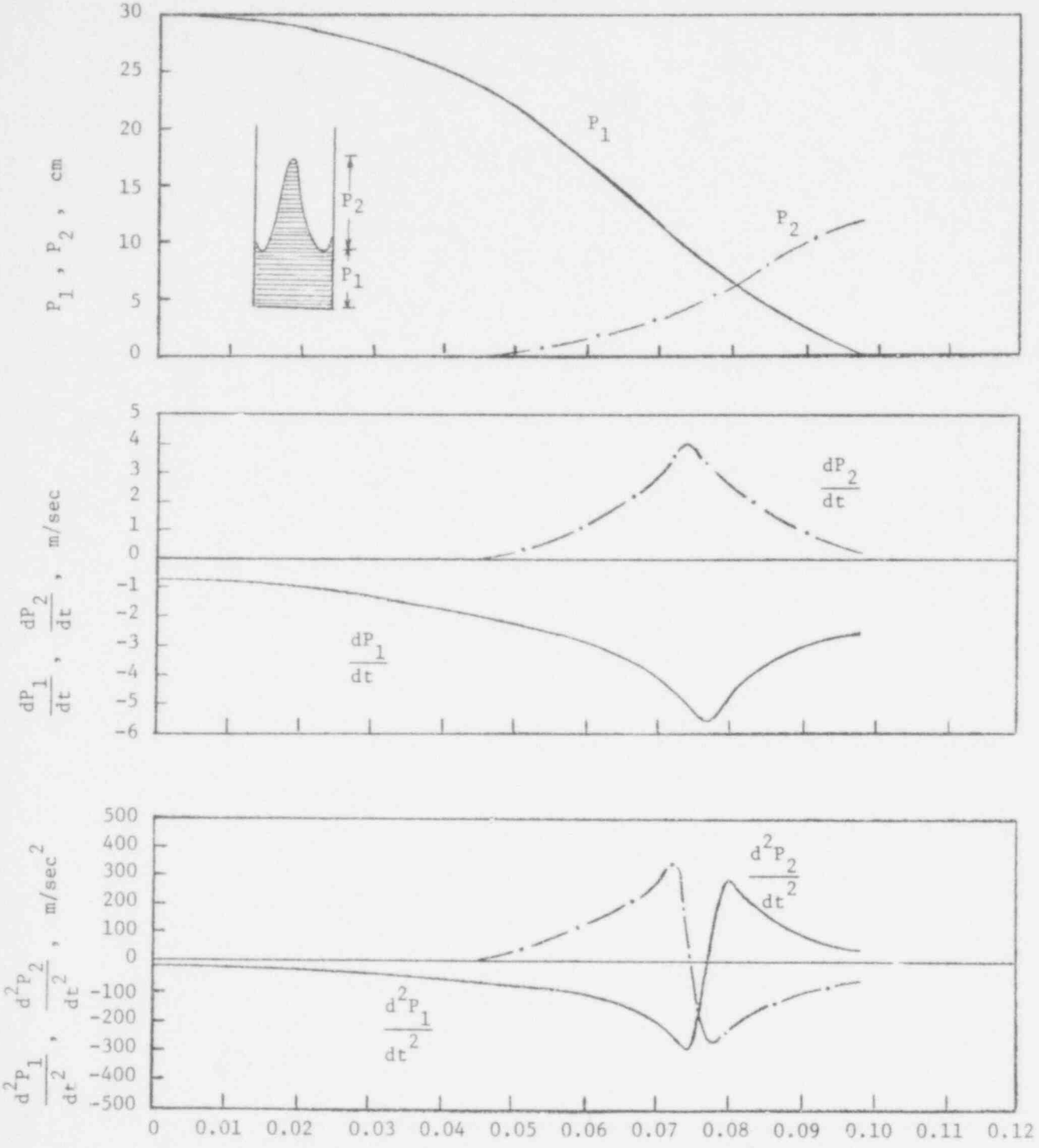

Fig. 3.2. Position, Velocity and Acceleration of the Air-Water Interfaces during Vent Clearing (46 mm ID Tube) with Upstream Pressure of 122.0 kPa.

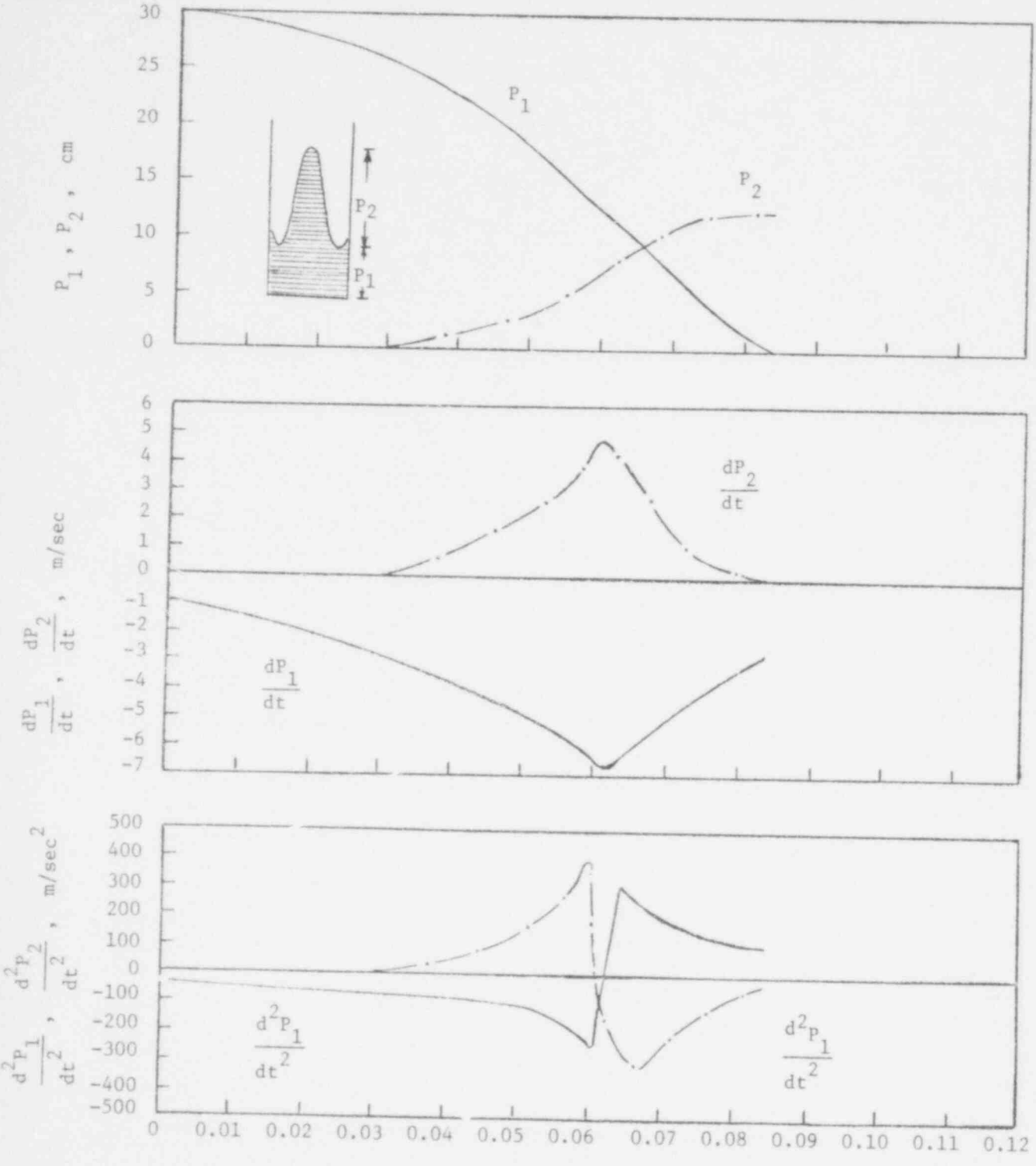

Fig. 3.3. Position, Velocity and Acceleration of the Air-Water Interfaces during Vent Clearing (46 mm ID Tube) with Upstream Pressure of 128.9 kPa.

the position, velocity and acceleration of the moving interface (P_1) as well as the liquid spike (P_2) standing above the interface. The data plotted in Figures 3.1-3.3 are for upstream pressures of 115, 122 and 129 kPa when the submergence depth of the 46 mm diameter tube was fixed to be 30 cm. The data for the interface heights were reduced from movies taken at 780 frames/sec. The height data were in turn used to calculate velocities and accelerations of the interfaces. The data for the acceleration is expected to suffer most from the data reduction errors but the maximum error should be less than ±25%.

From Figures 3.1-3.3 it is observed that the liquid spike grows monotonically with time but the growth rate slows down as the liquid spike attains a finite height. The velocity and acceleration of the liquid-gas interface (P_1) increase rapidly with time during the early stages of vent clearing but the interface slows down considerably during the later periods. The slowdown of the interface is probably caused by the additional drag induced by the liquid sticking to the tube wall, entrained in the tube and the drag at the surface of the liquid spike. The theoretical models [2] of the vent clearing phenomena do not account for these effects and for the same reasons these models predict a continuous increase in velocity and acceleration of the interface with time.

The data for the spike height (Figures 3.1-3.3) show that the liquid spike grows to about 12 cm before breaking up. Thus the linear theory as discussed earlier is bound to be inadequate. However, the linear theory can provide a starting point for further amplification of the phenomena. Knowing the acceleration of the liquid-air interface, the growth rate of the liquid spike can be written as

$$P_2 = P_{2o} e^{w(t)t} \tag{3.4}$$

where

$$w(t) = C_1 \sqrt[4]{\frac{(\rho_w + \rho_a)^2 g^3 \left[\frac{1}{g}\left|\frac{d^2P_1}{dt^2}\right| - 1\right]}{(\rho_w + \rho_a)}} \tag{3.5}$$

In Equation (3.4), P_{2o} is the initial height of the interface and is generally unknown. In the present case an appropriate choice for P_{2o} could be

$$P_{2o} = \sqrt{\sigma/[(\rho_w - \rho_a)g]}. \tag{3.6}$$

This gives a value of 0.25 cm for P_{2o} at earth normal gravity and for a water-air interface and room temperature. This value of P_{2o} is also about the height of the interface which could be discerned from the movies. The constant in Equation (3.5) is expected to be less than 0.6 because in the early stages the growth rate corresponding to shorter and slower waves may be more favorable. The dimensionless liquid spike height (P_2/P_{2o}) corresponding to upstream pressures of 115, 122 and 129 kPa is plotted in Figures 3.4, 3.5 and 3.6 as a function of time. It is seen that during the early stages of the growth of the interface, when d^2P_1/dt^2 changes slowly with time, the linear theory can be used to predict the spike height. The constant C_1 from the three observations is found to be 0.16 ±0.2. The linear theory becomes more and more inaccurate as the liquid spike grows to a finite height.

3.1.1. Application to Vent Clearing in a BWR Suppression Pool

The acceleration of the water-air interface during vent clearing in a BWR suppression pool [2] is plotted in Figure 3.7. Though the maximum acceleration experienced by the liquid is much less than that observed in laboratory experiments, it is about six times greater

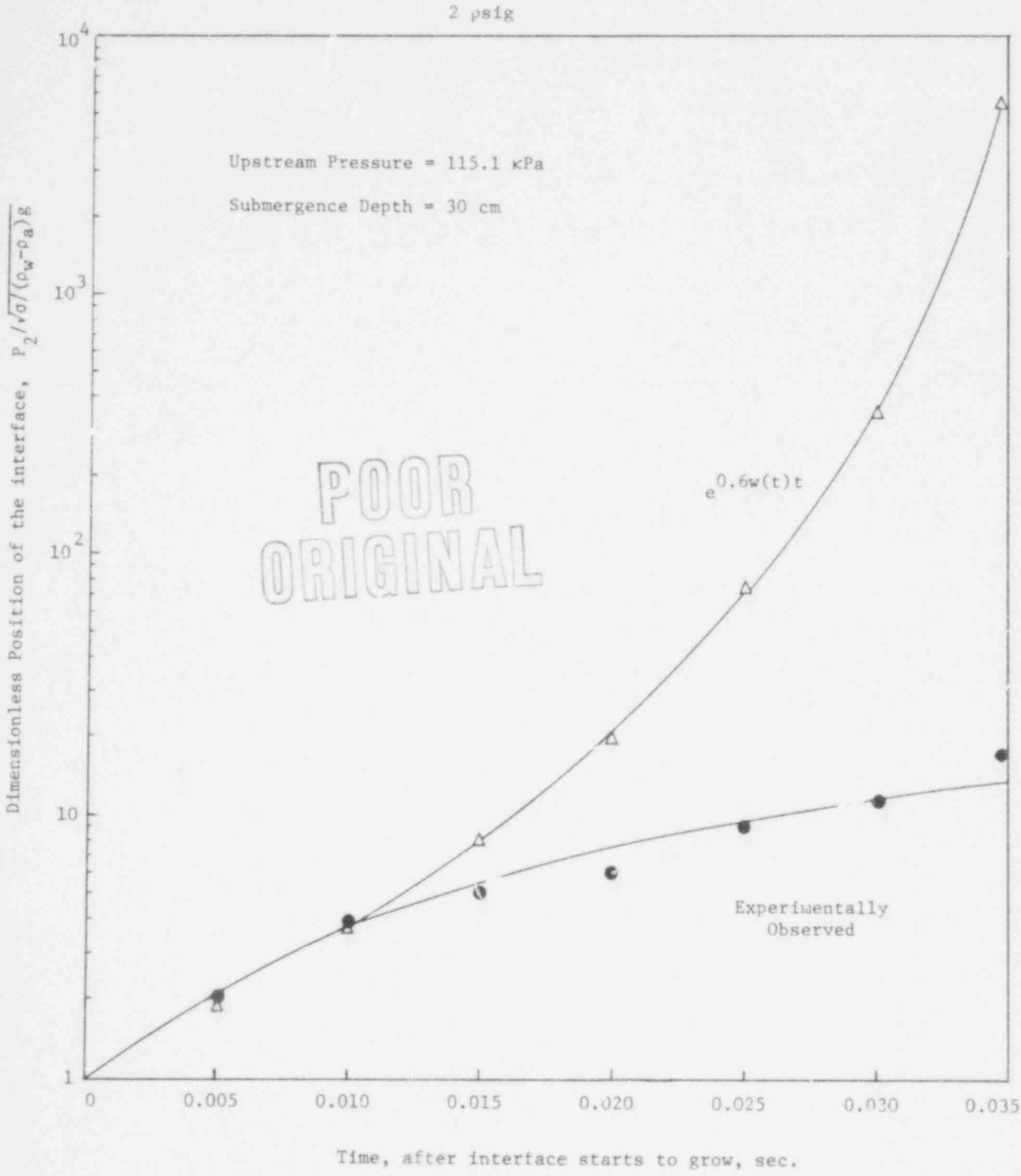

Fig. 3.4. Growth rate of the interface in 46 mm diameter tube with upstream pressure of 115.1 kPa.

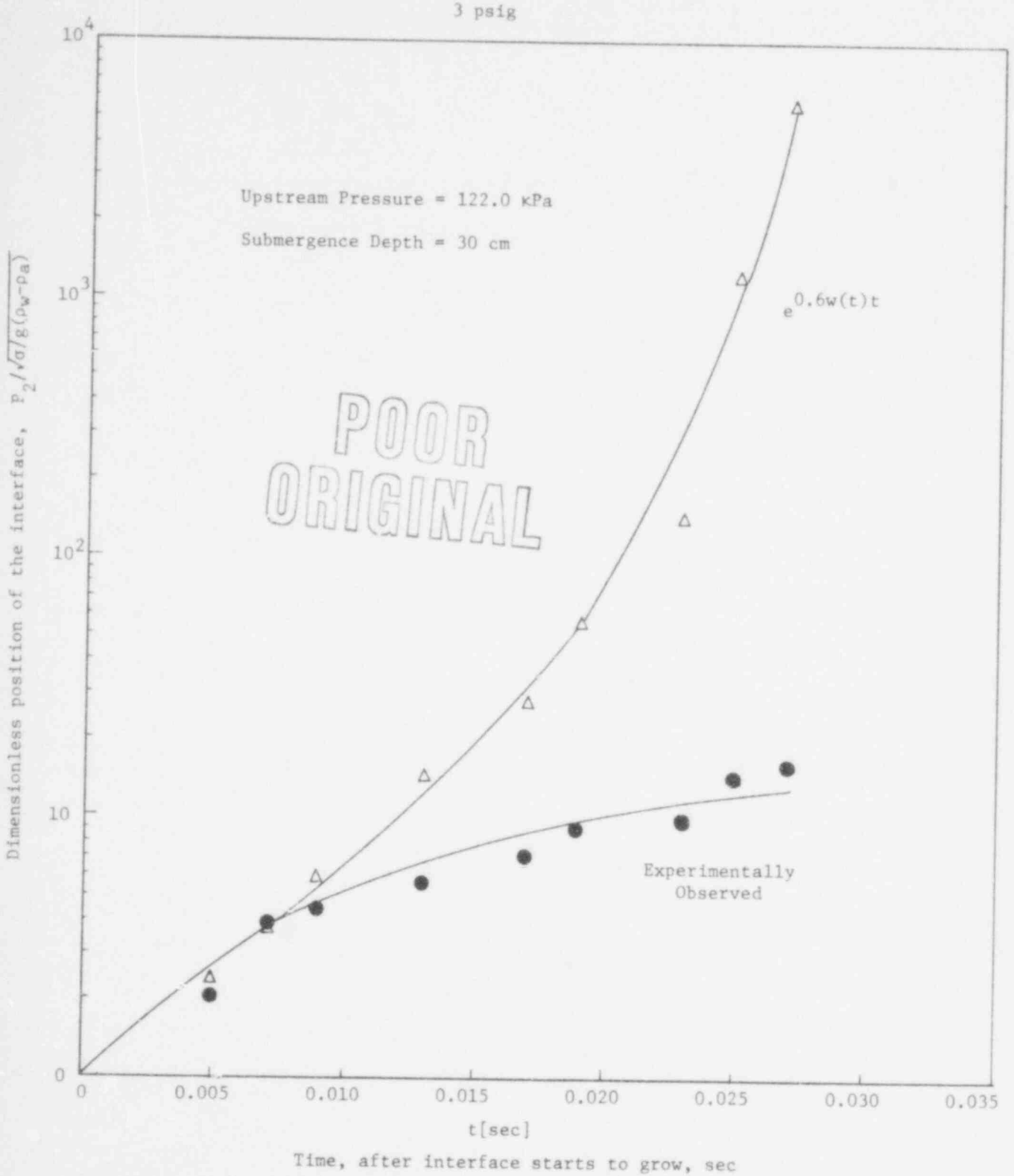

Fig. 3.5. Growth rate of the interface in 46 mm diameter tube with upstream pressure of 122 kPa.

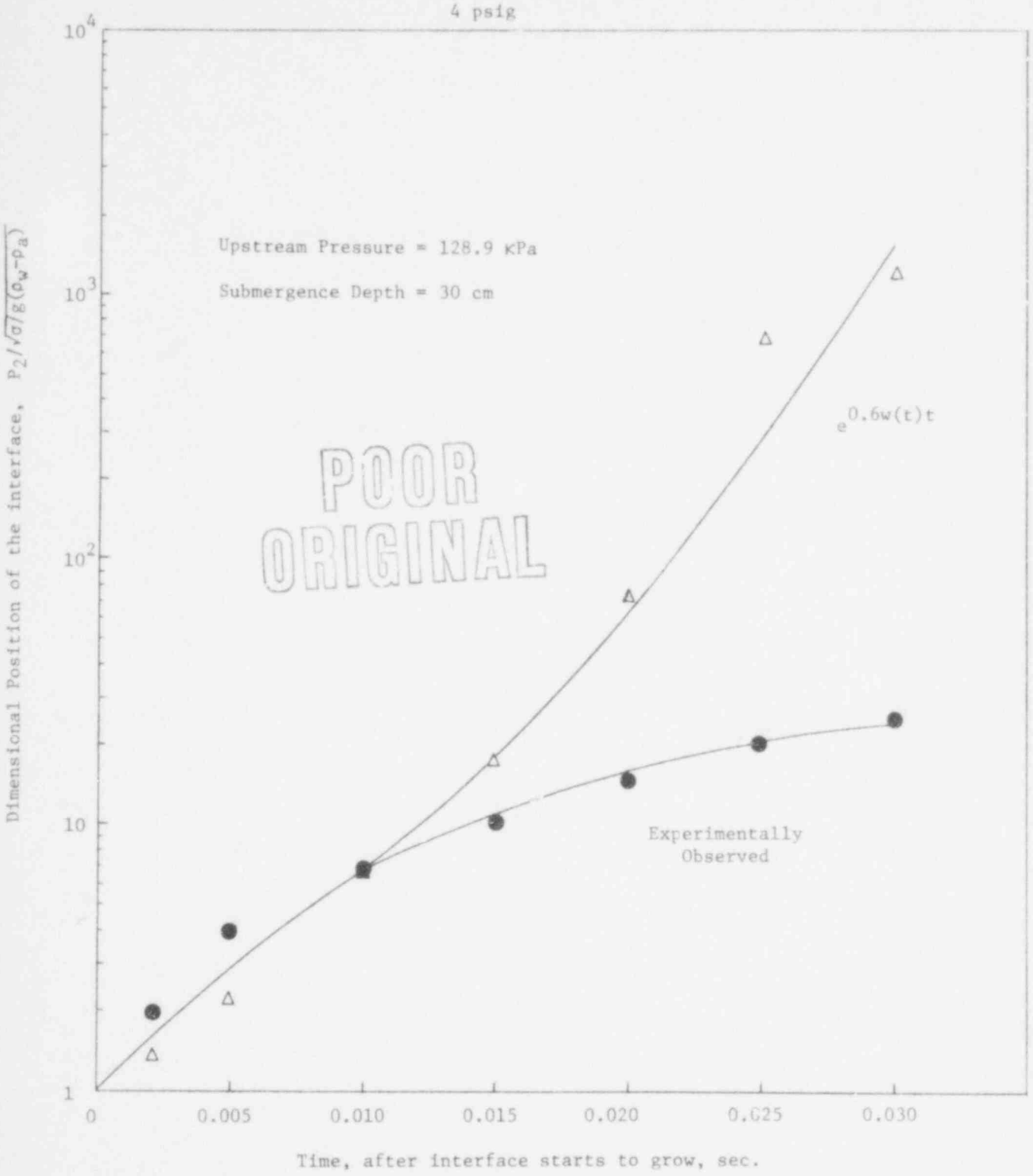

Fig. 3.6. Growth rate of the interface in 46 mm diameter tube.

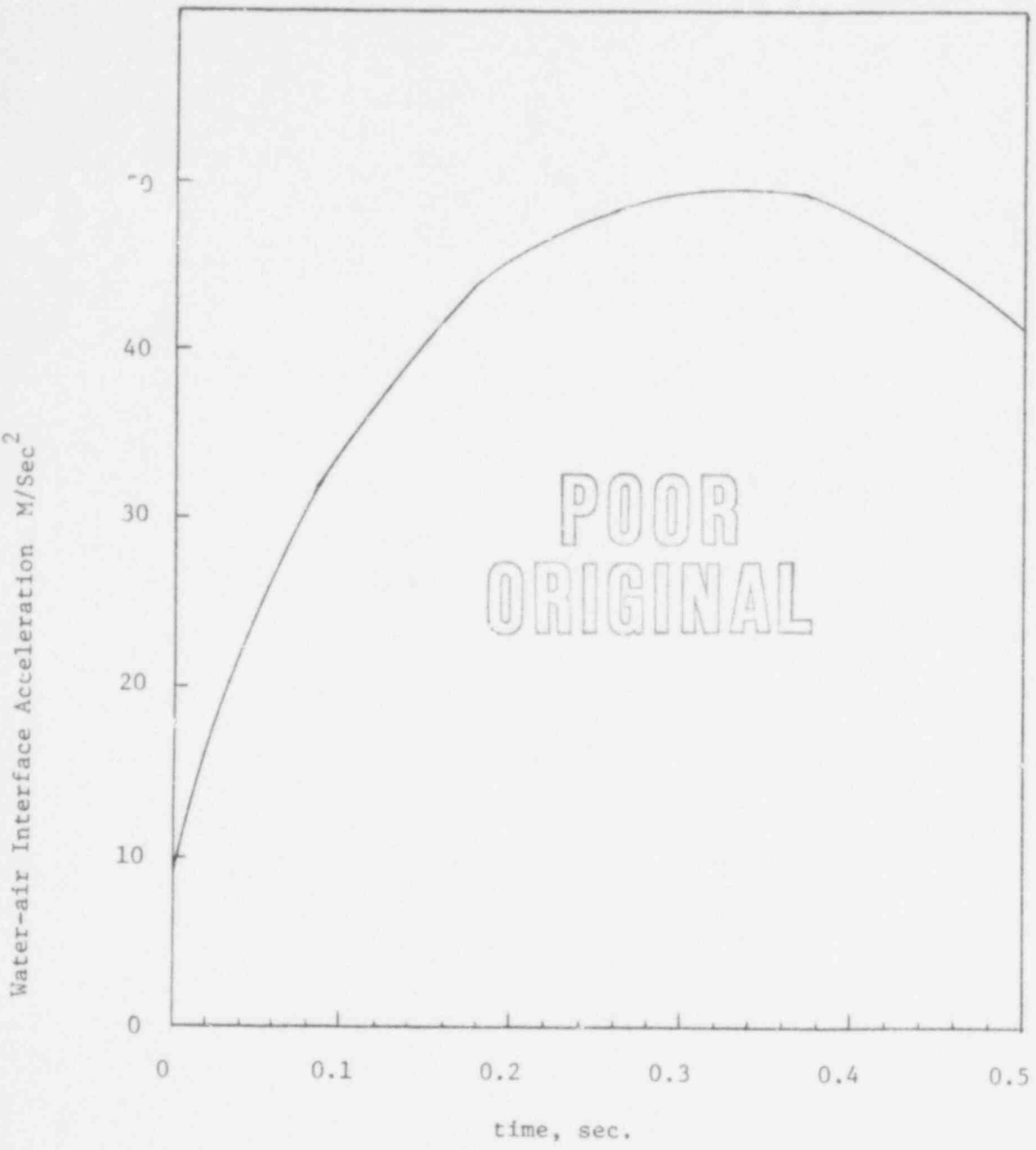

Fig. 3.7. Predicted acceleration of the interface during Vent Clearing ina BWR Suppression pool.

in magnitude than earth normal gravity. The instabilities at the interface will start to grow when the acceleration of the interface is such that the shortest unstable wavelength can be accommodated in the vent. For a 0.6 meter diameter vent, the acceleration of the interface needs to be only 9.85 m/sec^2 for the interface to start to grow. However, as the acceleration of the interface exceeds this value, the wavelength of the unstable waves will become shorter and a number of liquid spikes may be observed to grow on the moving interface. The growth rate of a liquid spike predicted by linear theory is shown in Figure 3.8.

3.2. Bubble Formation and Growth

High speed movies of the air bubble growing at the vent exit were made for different upstream pressures and submergence depths. Figures 3.9, 3.10 and 3.11 show the sketches of the growth pattern of a bubble at the exit plane of a 16 mm tube for upstream pressures of 115.1, 128.9 and 142.7 kPa while the submergence depth was fixed at 10 cm. The last sketch in each Figure shows the bubble shape and size prior to bubble break-up. The bubble is observed to grow spherically only for a very short period of time and soon the bubble shape is controlled by a balance between gravity and inertial forces. The inertial forces tend to elongate the bubble while the buoyancy force tends to flatten it. As a result the bubble acquires a strawberry shape with the maximum diameter to height ratio of the bubble decreasing with higher upstream pressures. The growth patterns of the bubbles for submergence depths of 30 and 45 cm are shown in Figures 3.12-3.14 and Figures 3.15-3.17. Higher submergence depth is seen to enhance the buoyancy effect and thereby tends to flatten

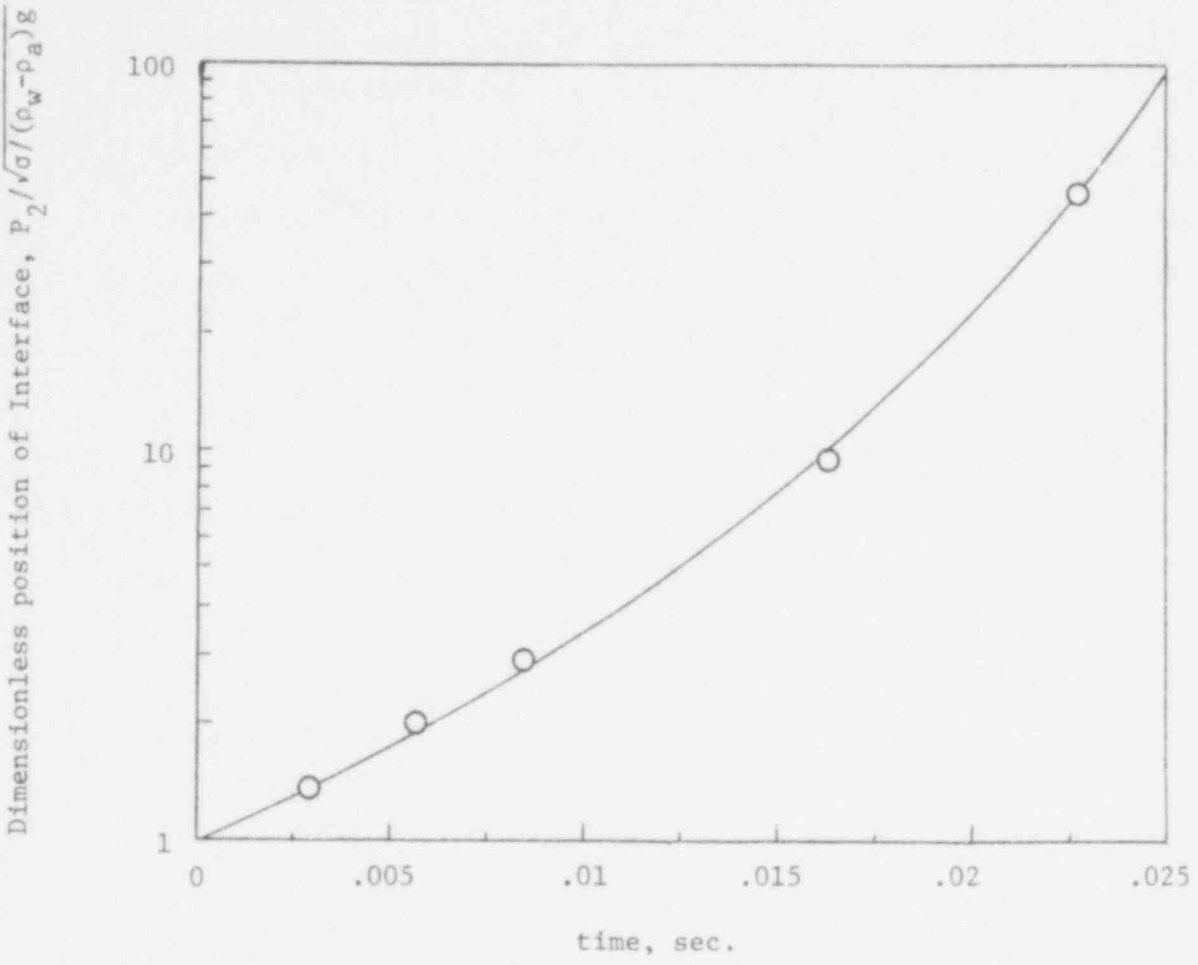

Fig. 3.8. Predicted growth rate of interface during Vent Clearing in a BWR Suppression pool.

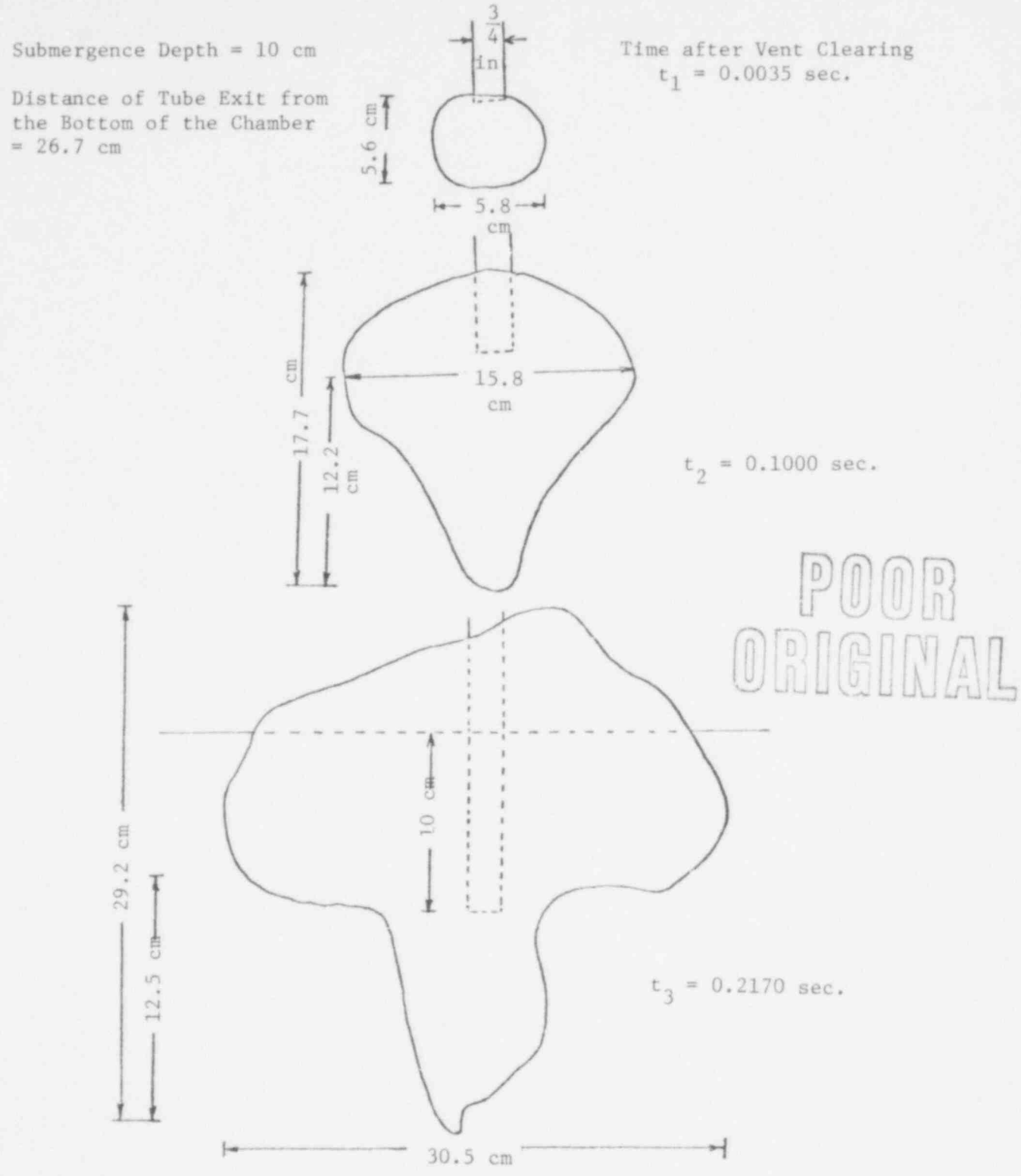

Fig. 3.9. History of Bubble Growth at the Exit of a 1.59 cm I.D. Tube with Upstream Pressure of 115.1 κ Pa.

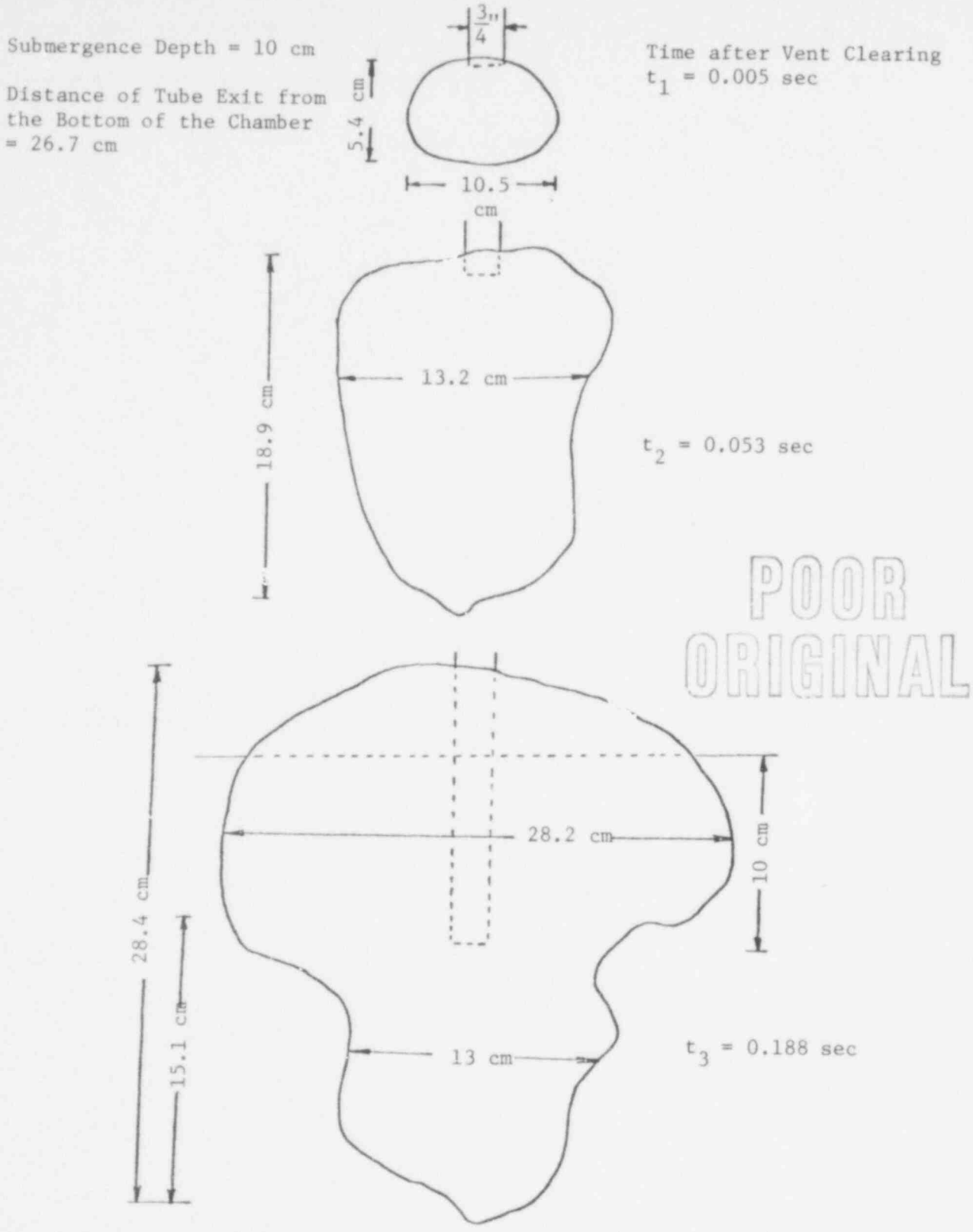

Fig. 3.10. History of Bubble Growth at the Exit of a 1.59 cm I.D. Tube with Upstream Pressure of 128.9 κ Pa.

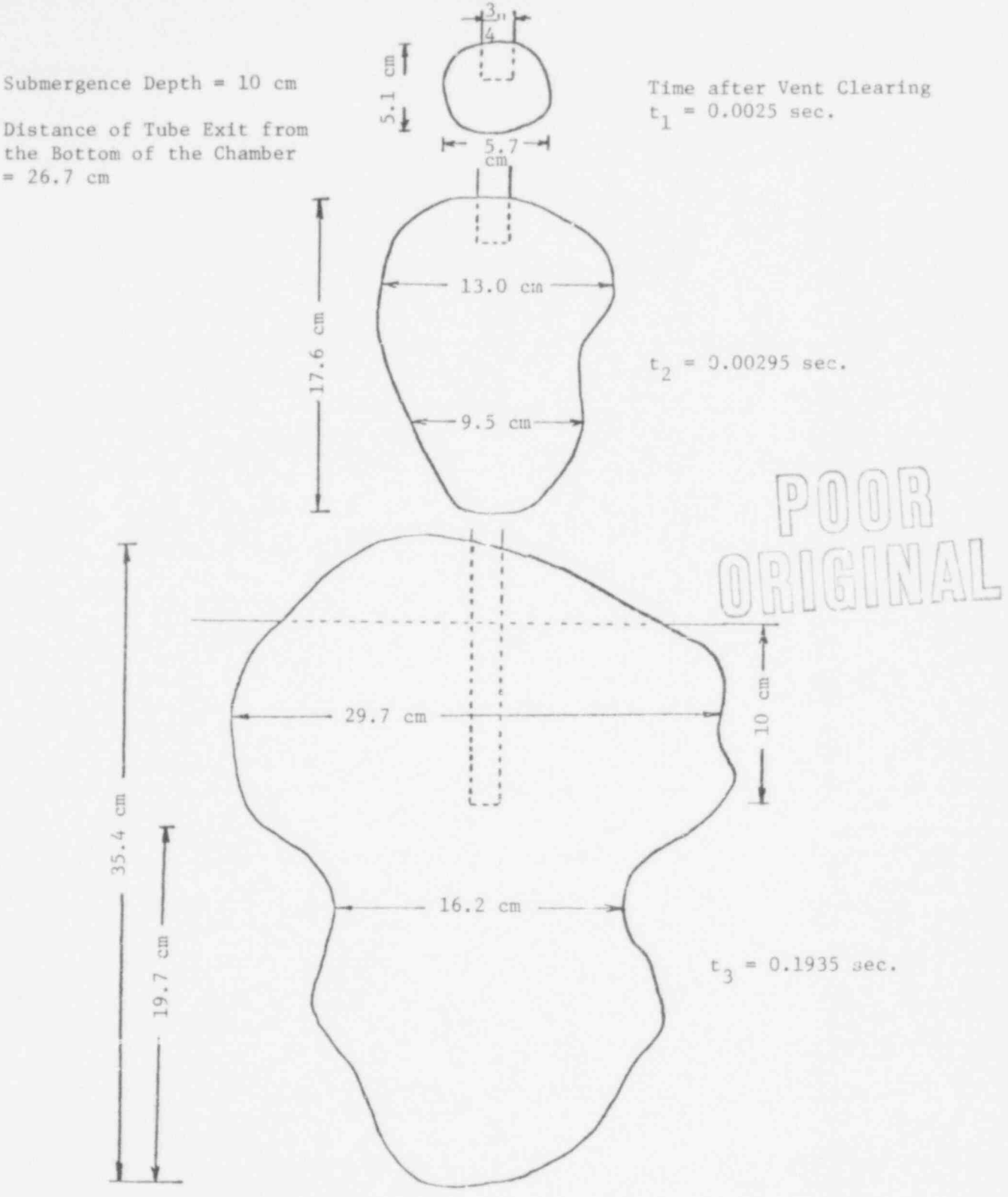

Fig. 3.11. History of Bubble Growth at the Exit of a 1.59 cm I.D. Tube with Upstream Pressure of 142.7 κ Pa.

Submergence Depth = 30 cm

Distance of Tube Exit from the Bottom of the Chamber = 26.7 cm

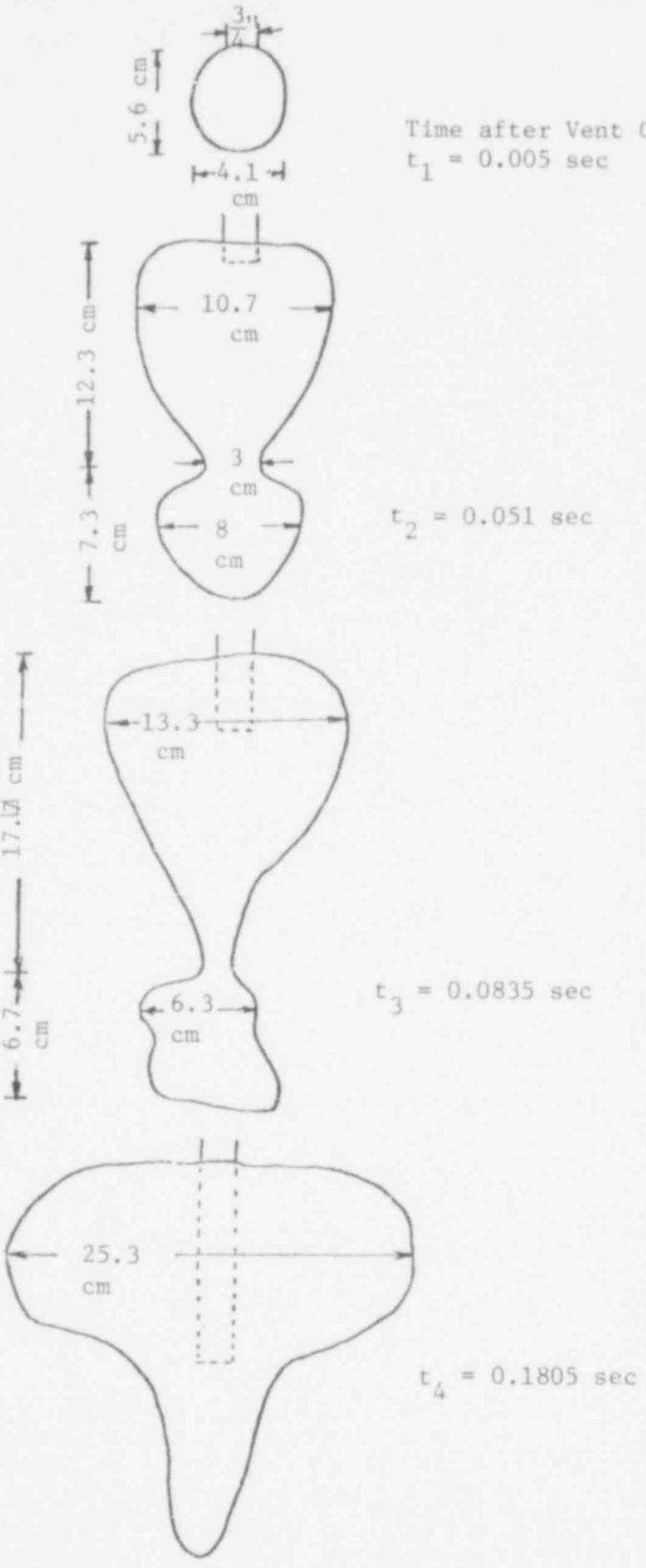

Fig. 3.12. History of Bubble Growth at the Exit of a 15.9 cm I.D. Tube with Upstream Pressure of 115.1 kPa (Continued on Following Page).

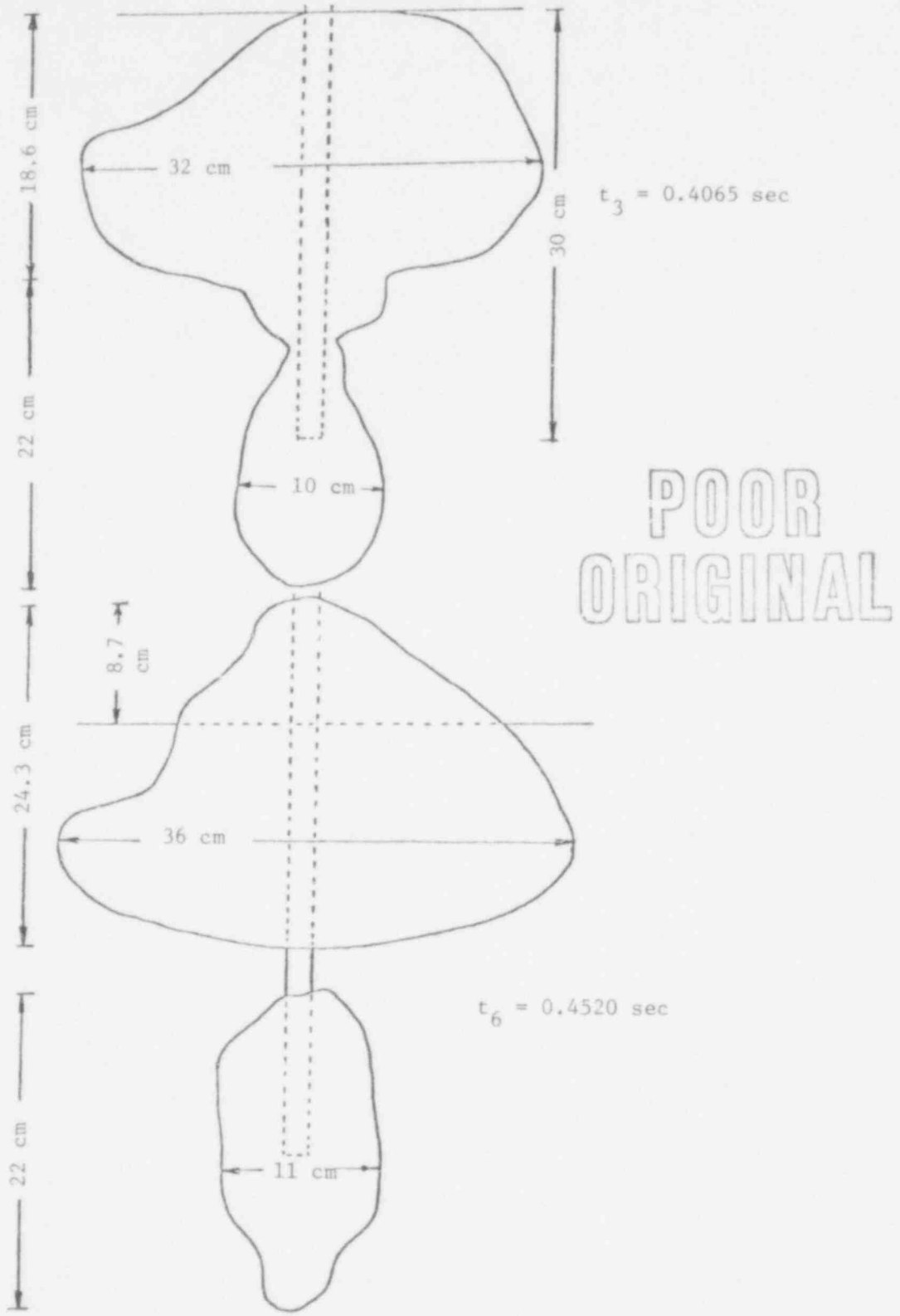

Fig. 3.12. History of a bubble Growth at the Exit of a 1.59 cm I.D. Tube with Upstream Pressure of 115.1 κ Pa (Continued from Previous Page).

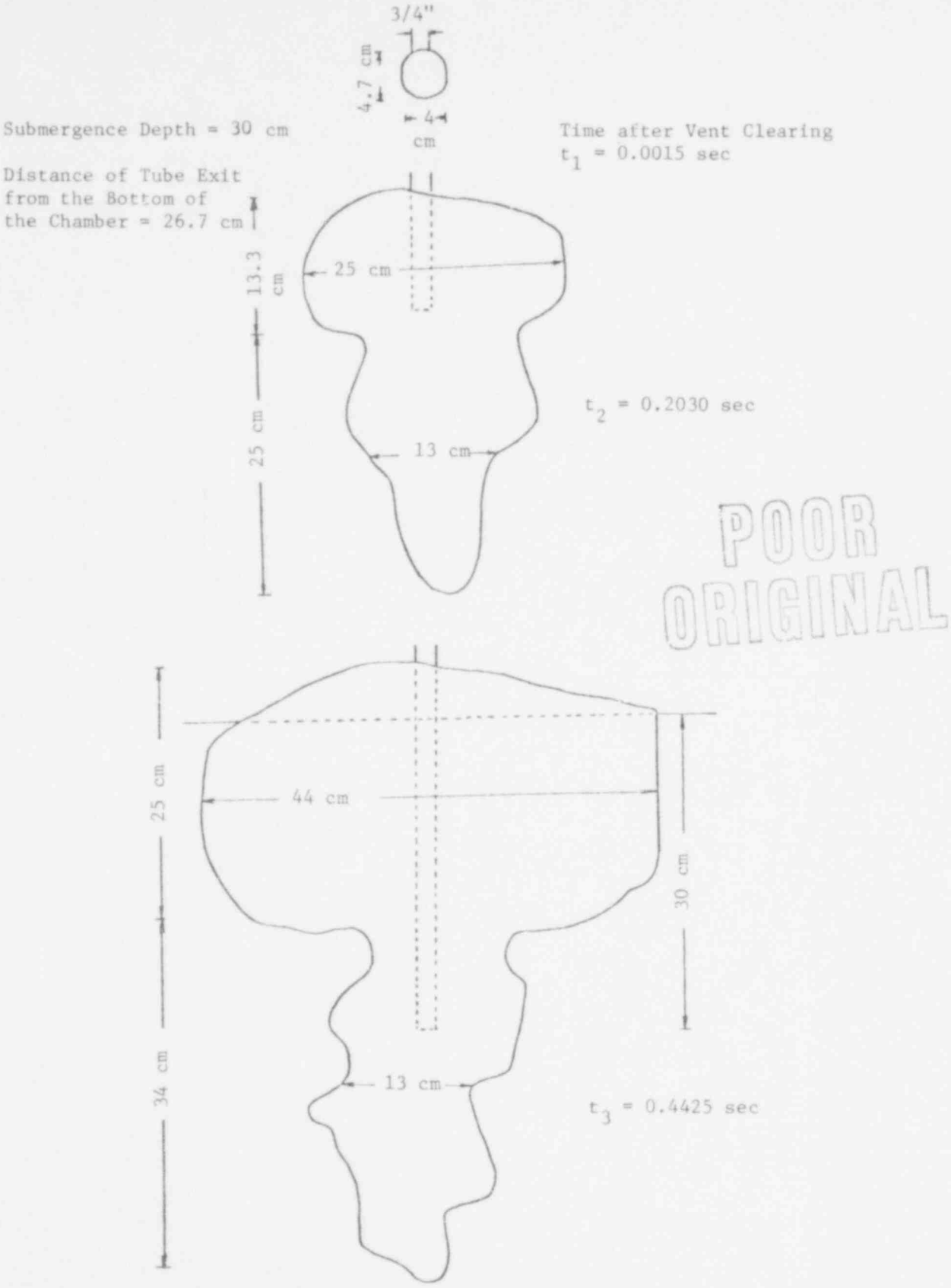

Fig. 3.13. History of Bubble Growth at the Exit of a 15.9 cm I.D. Tube with Upstream Pressure of 128.9 κ Pa.

Submergence Depth = 30 cm

Distance of Tube Exit from the Bottom of the Chamber = 26.7 cm

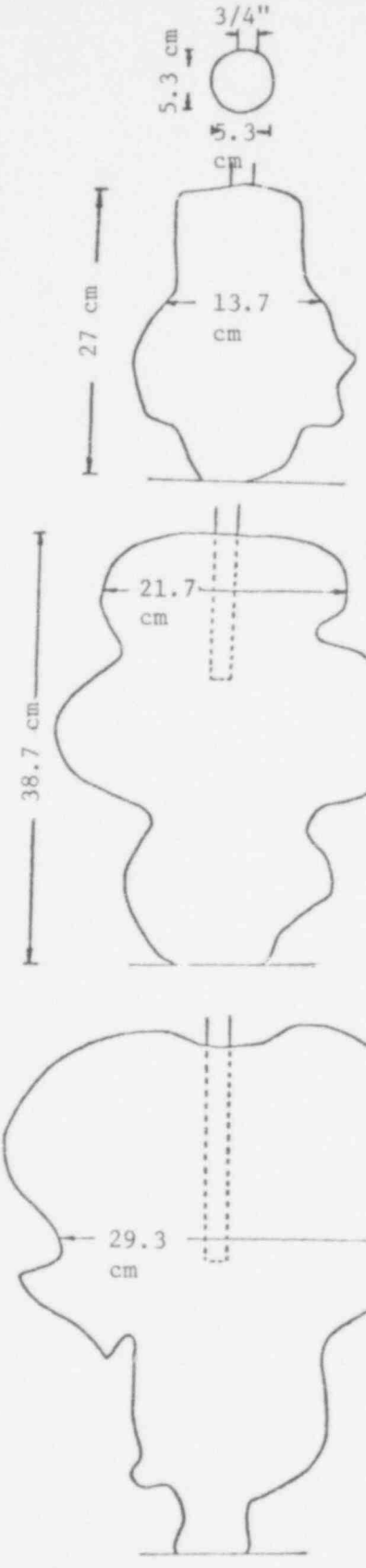

Time after Vent Clearing

t_1 = 0.00175 sec

t_2 = 0.0705 sec

t_3 = 0.2145 sec

t_4 = 0.3085 sec

3.14. History of Bubble Growth at the Exist of a 1.59 cm I.D. Tube with Upstream Pressure of 142.7 kPa (Continued on Following Page).

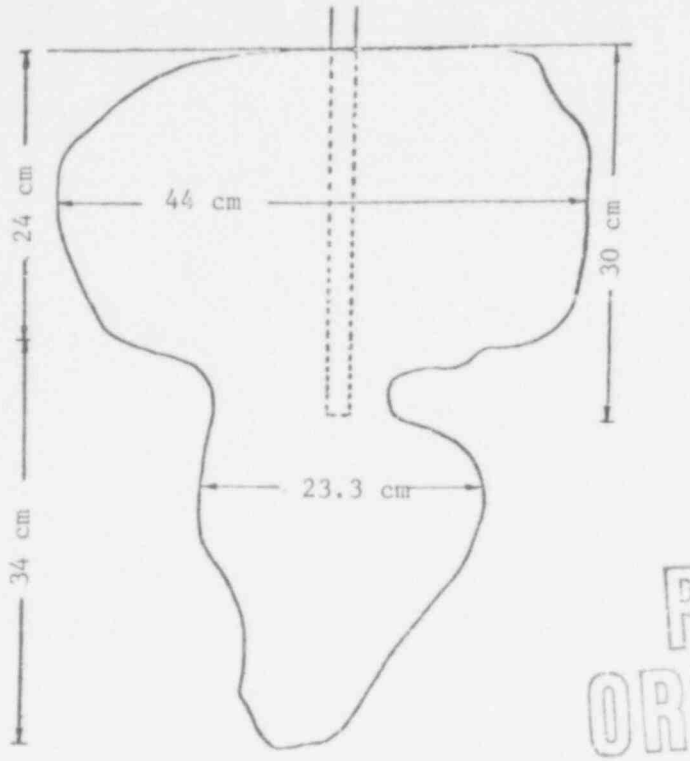

t_5 = 0.4230 sec

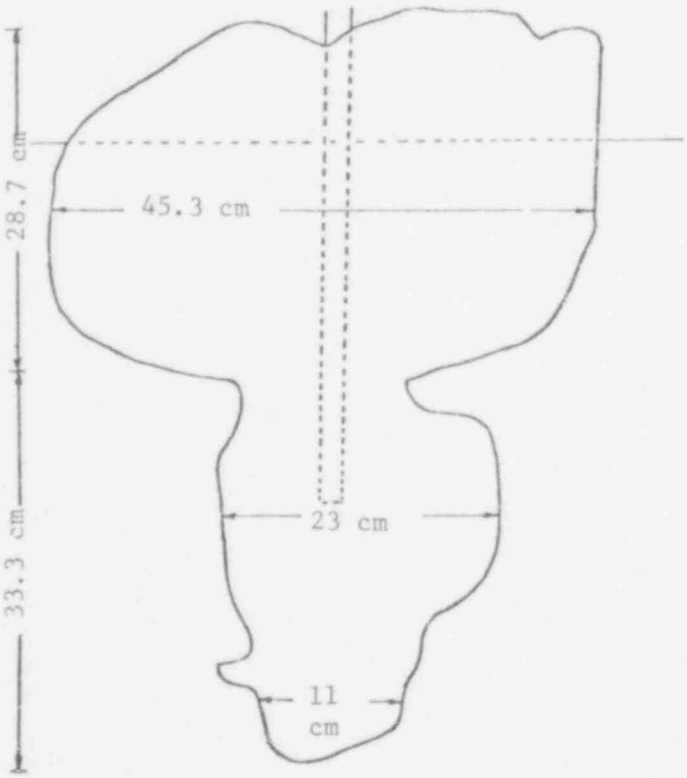

Fig. 3.14. History of Bubble Growth at the Exit of a 1.59 cm I.D. Tube with Upstream Pressure of 142.7 κ Pa (Continued from Previous Page).

Submergence Depth = 45 cm

Distance of Tube Exit from the Bottom of the Chamber = 26.7 cm

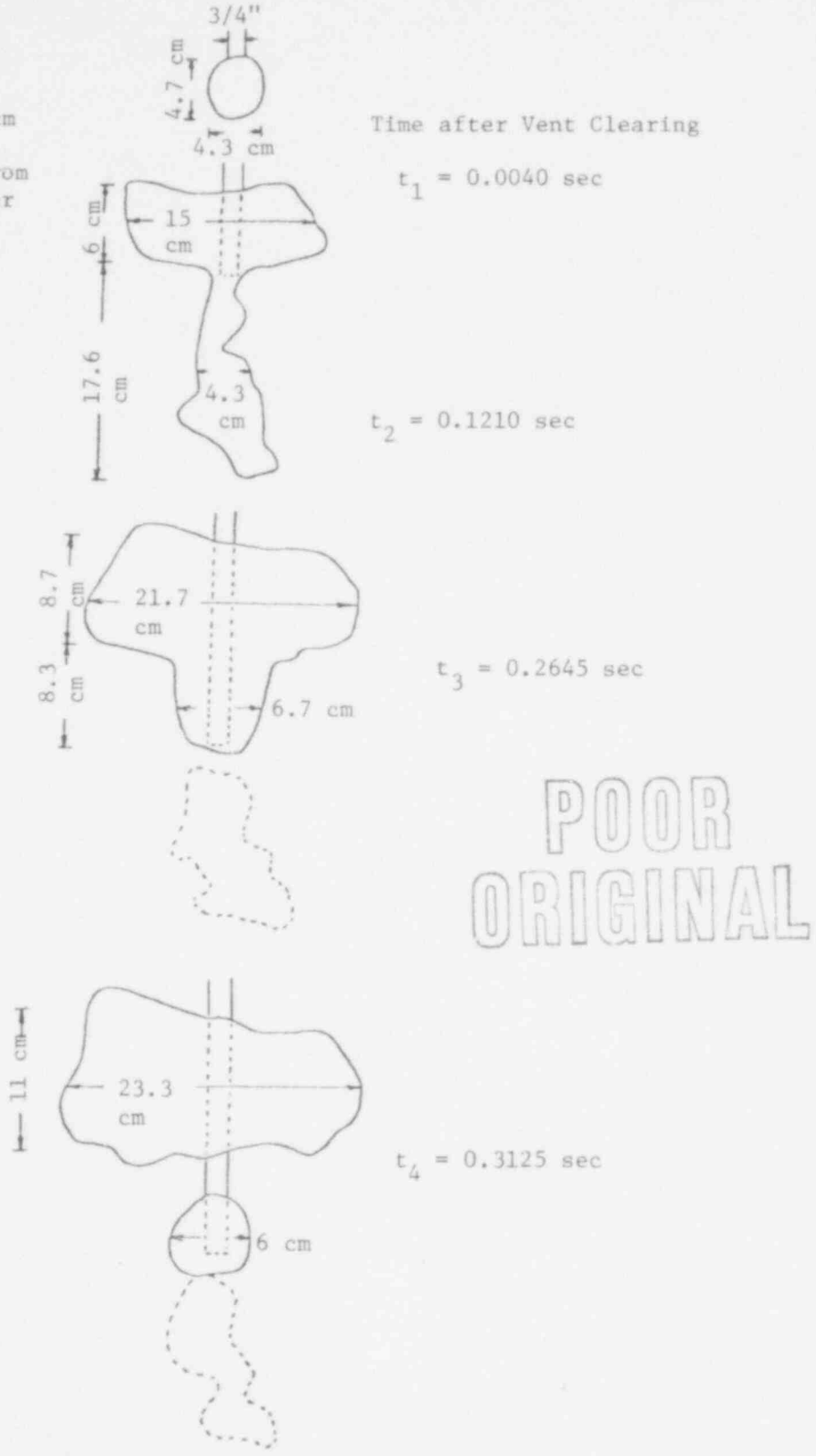

Fig. 3.15. History of Bubble Growth at the Exit of a 1.59 cm I.D. Tube with Upstream Pressure of 115.1 kPa (Continued on Following Page).

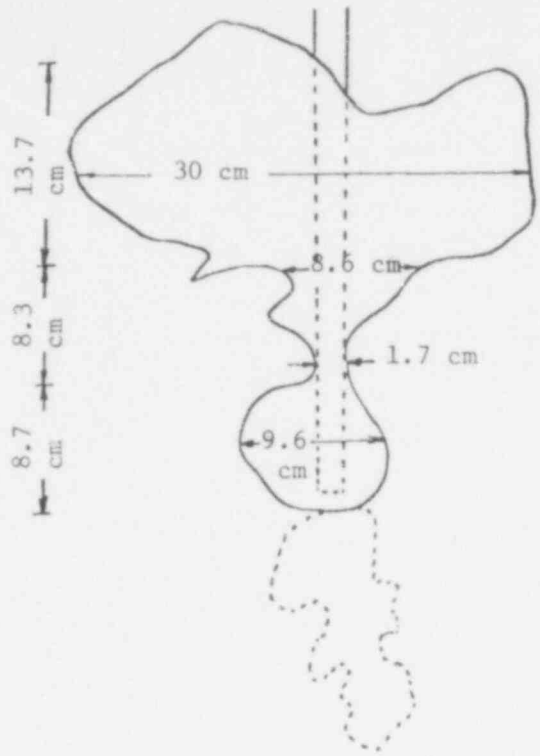

t_5 = 0.4840 sec

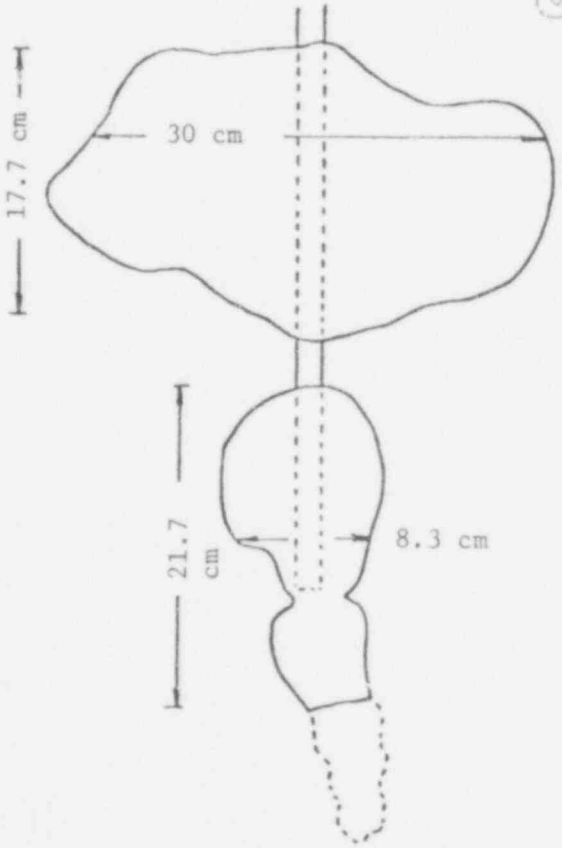

t_6 = 0.5360 sec

Fig. 3.15. History of Bubble Growth at the Exit of a 1.59 cm I.D. Tube with Upstream Pressure of 115.1 κ Pa (Continued from Previous Page).

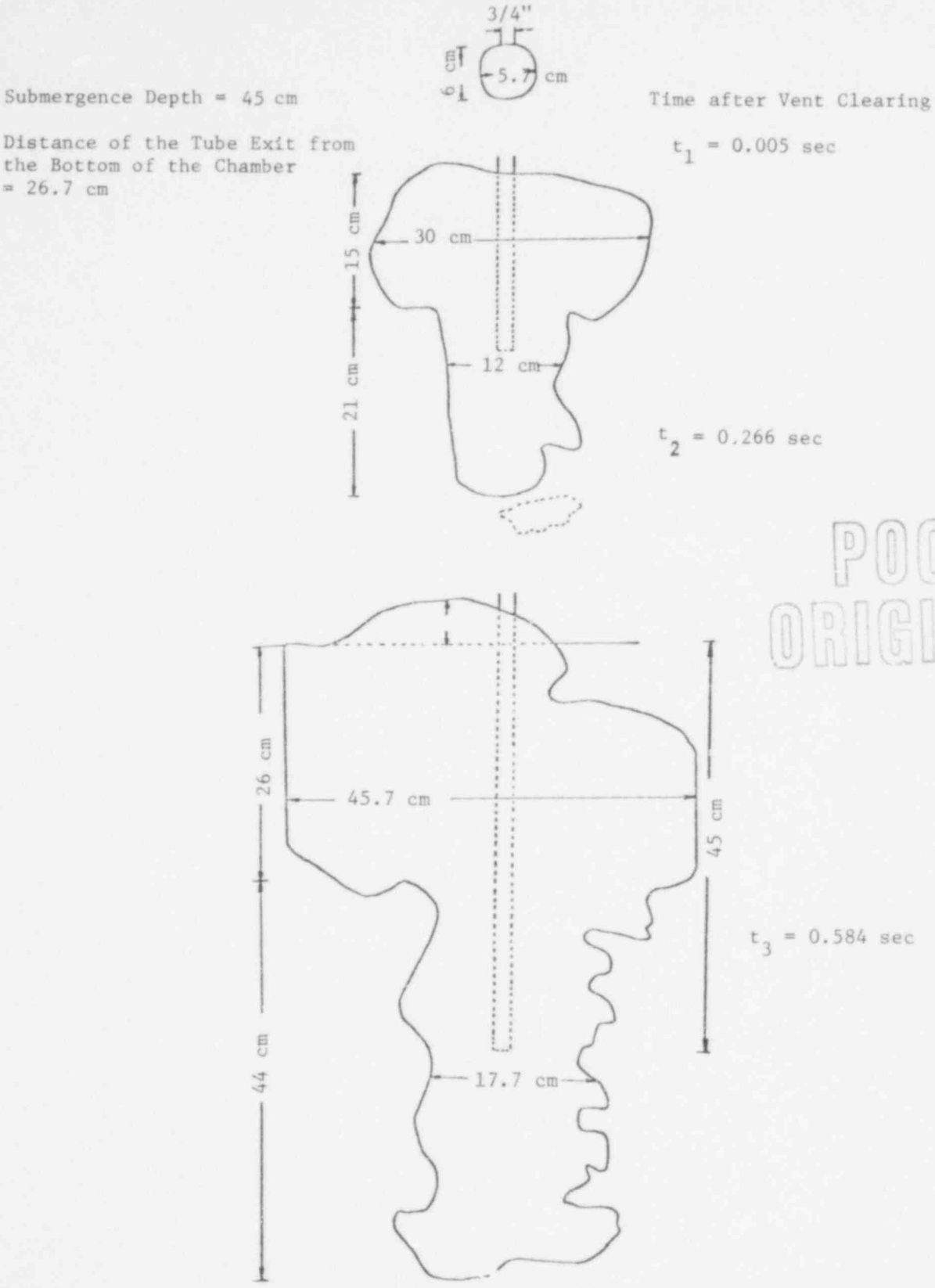

Fig. 5.16. History of Bubble Growth at the Exit of a 1.59 cm I.D. Tube with Upstream Pressure of 128.9 κ Pa.

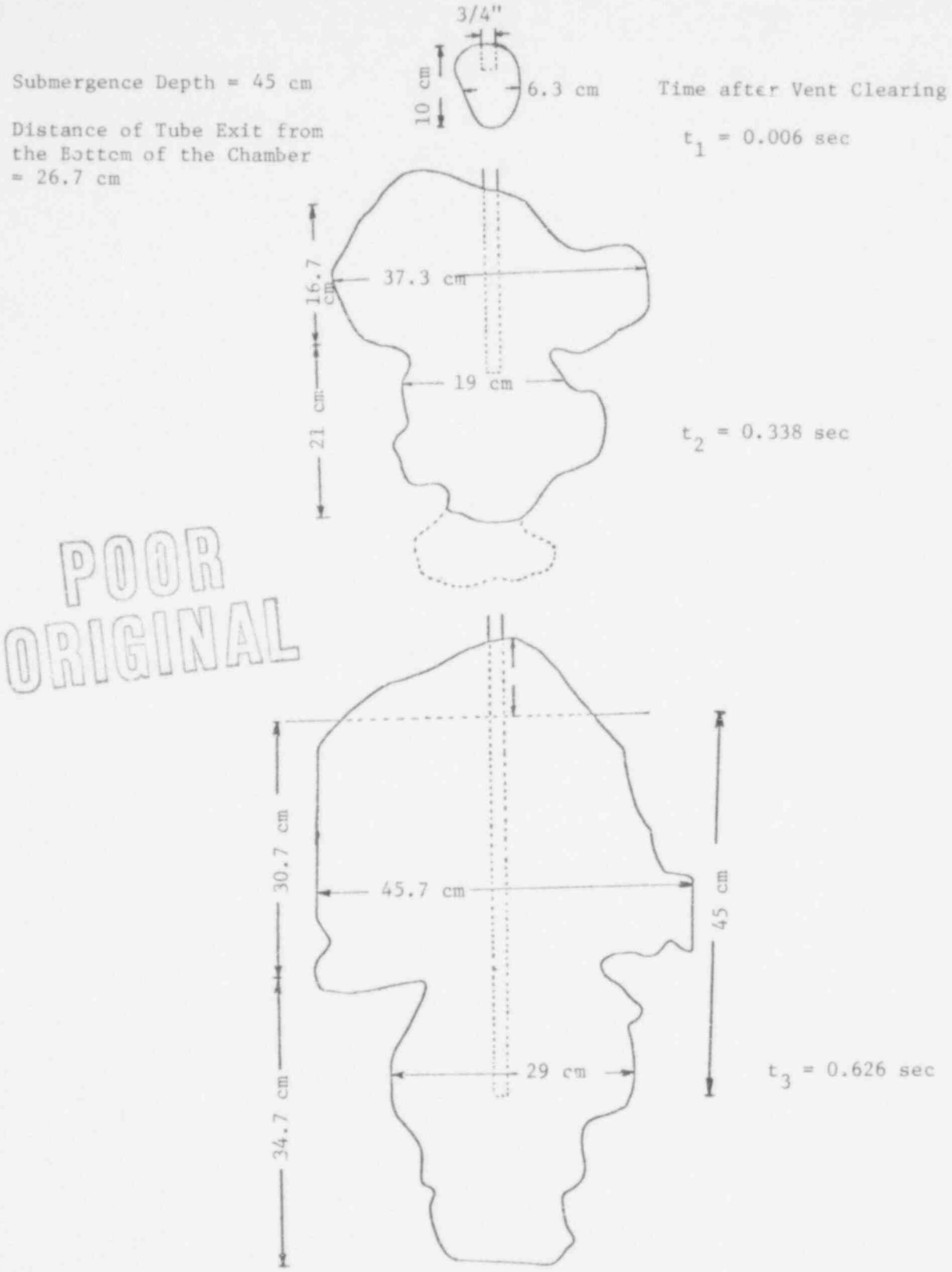

Fig. 3.17. History of Bubble Growth at the Exit of a 1.59 cm I.D. Tube with Upstream Pressure of 142.7 κ Pa.

the bubbles. The time taken by the bubbie to attain a finite size prior to leaving the vent is also seen to depend on the submergence depth. The main features of the bubble, however, remain unchanged. The ratio of bubble diameter to bubble height (aspect ratio) is plotted against upstream pressure in Figure 3.18. It is observed that the bubble aspect ratio decreases with Froude number and increases with submergence depth. Assuming the bubble to be a body of revolution in the plane of the picture, the bubble volume was calculated as a function of time. It is seen from Figure 3.19 that the bubble volume increases with upstream pressure and submergence depth.

3.3. Dynamical Force on Pool Bottom

After vigorous testing of different pressure transducers (see Appendix B), the Statham differential pressure transducer, model PM 131TC, was found to have the best response. It was then installed in the middle of the bottom plate of the cylindrical tank for detecting the total dynamical pressure. Typical pressure responses are shown in Figures 3.20, 3.21 and 3.22. Figure 3.23 illustrates the various stages of bubble growth during vent clearing, keyed to corresponding points on the pressure traces.

3.4. Preliminary Design for the Steam Injection Experiment

3.4.1. Design Criteria

A facility is currently under design in which steam can be discharged through a single vent pipe under the surface of a water pool. Experimental data will be obtained in this facility for various parameters of interest on the suppression of steam by the water pool. These parameters include steam mass flux, pool water temperatures, steam enthalpy, and the effect of dissolved air in the pool water. The effect of air in

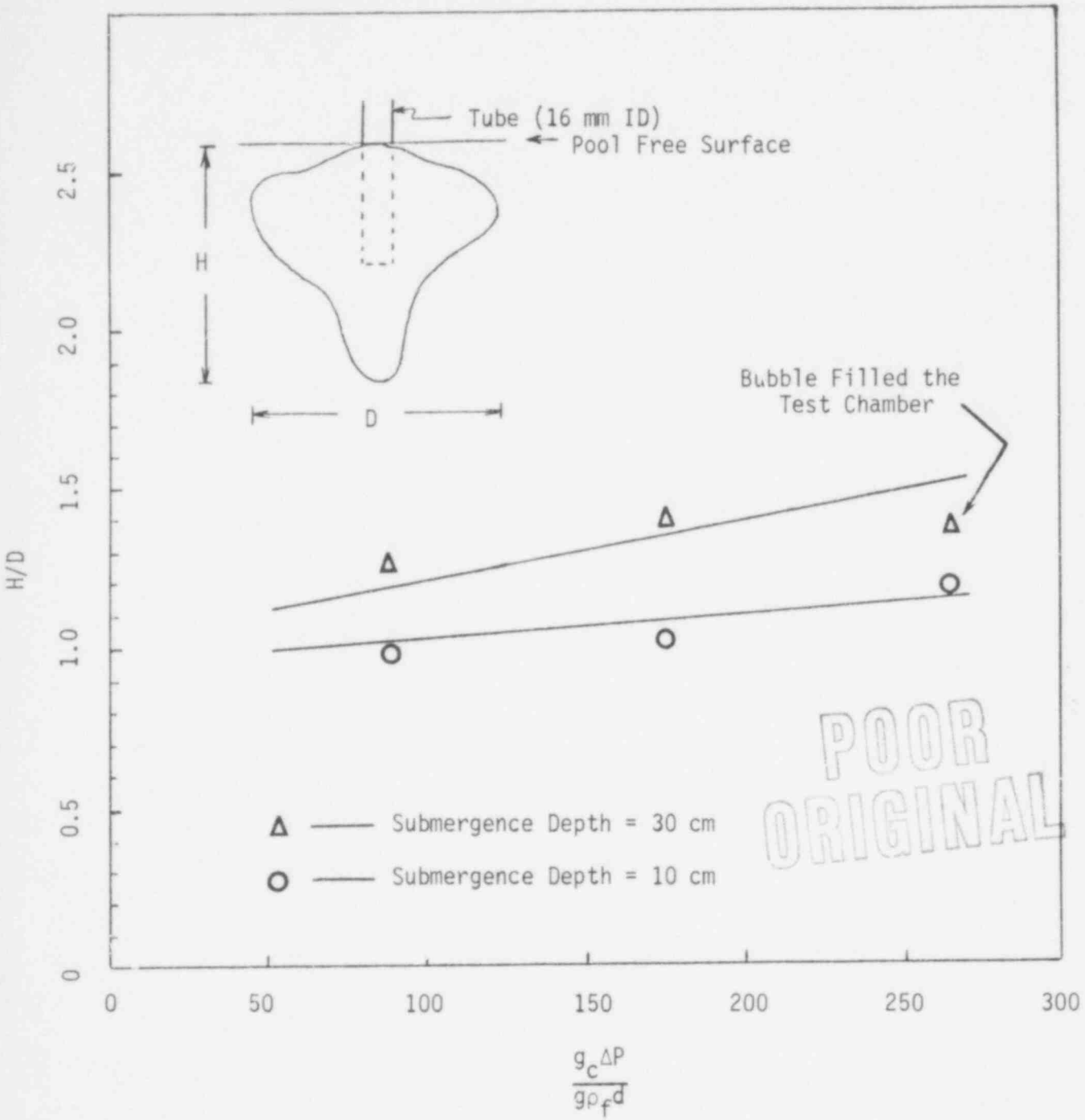

Figure 3.18.

Dependence on Upstream Pressure

of Bubble Aspect Ratio prior to Departure.

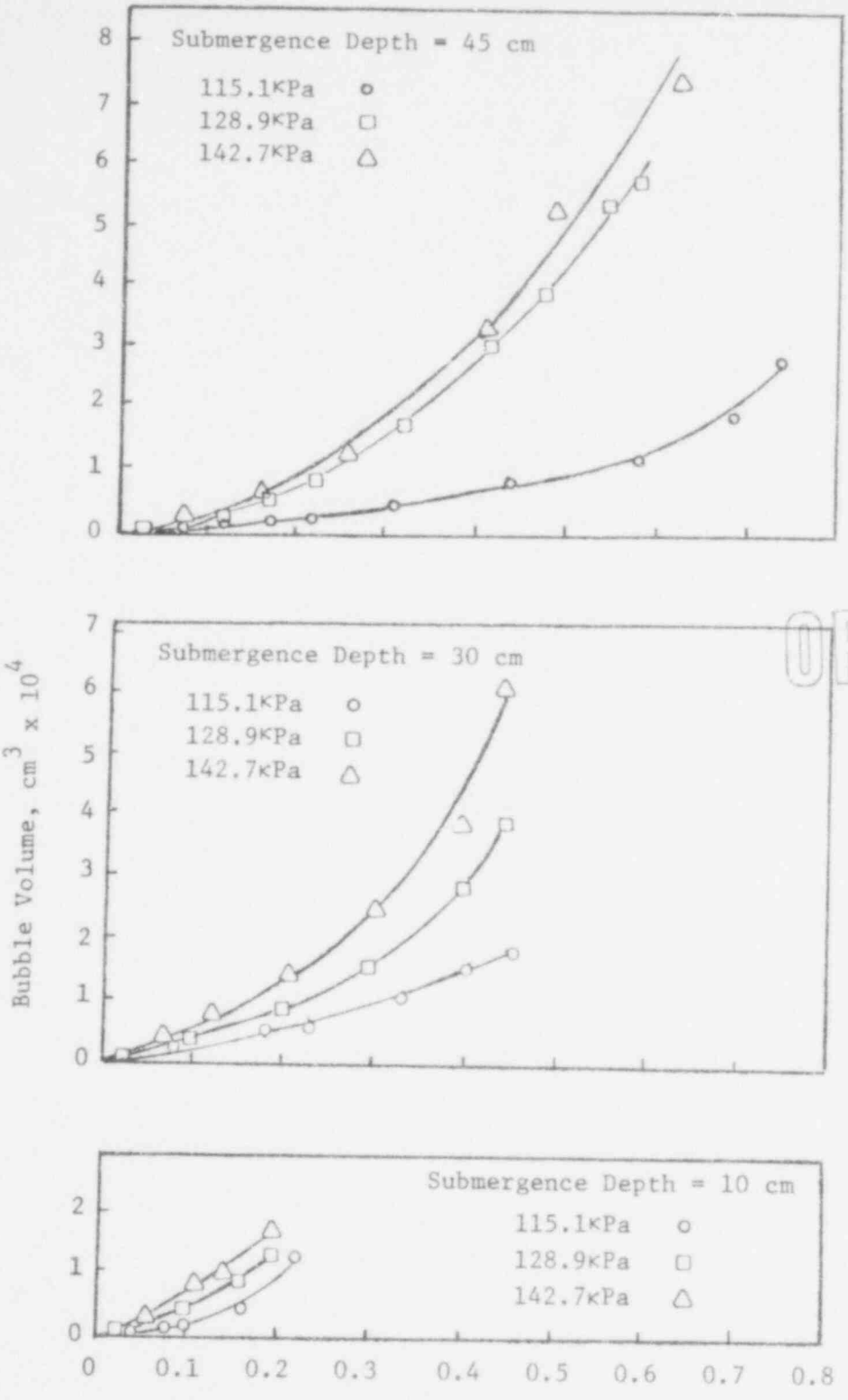

Fig. 3.19. Dependence on Time of the Volume of the Air Bubble at the Exit of 16 mm I.D. Tube.

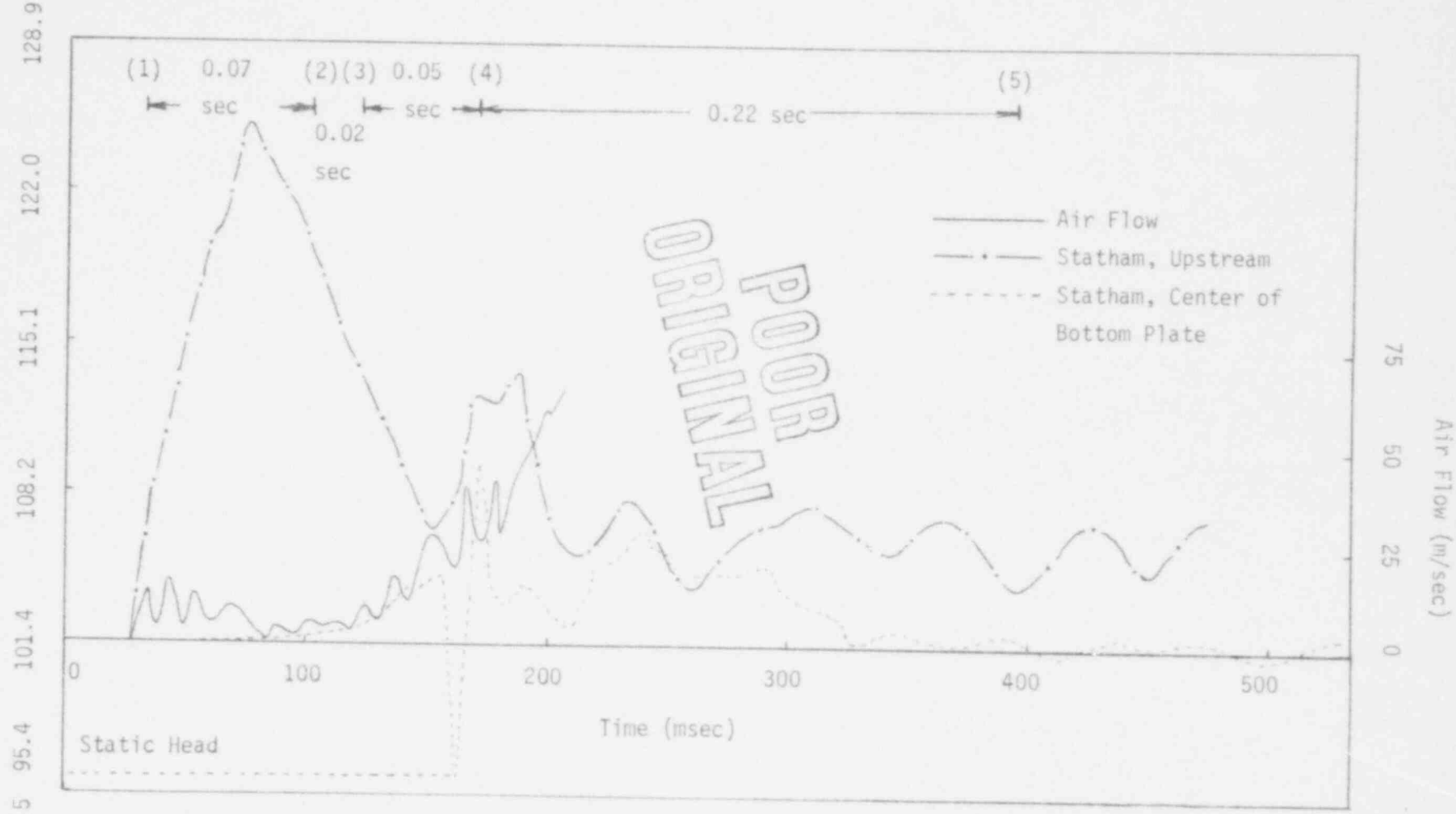

Figure 3.20. Pressure Forces Generated on the Upstream and the Bottom Plate during Vent Clearing (4.6 cm ID Tube) with Upstream Pressure of 122.0 kPa.

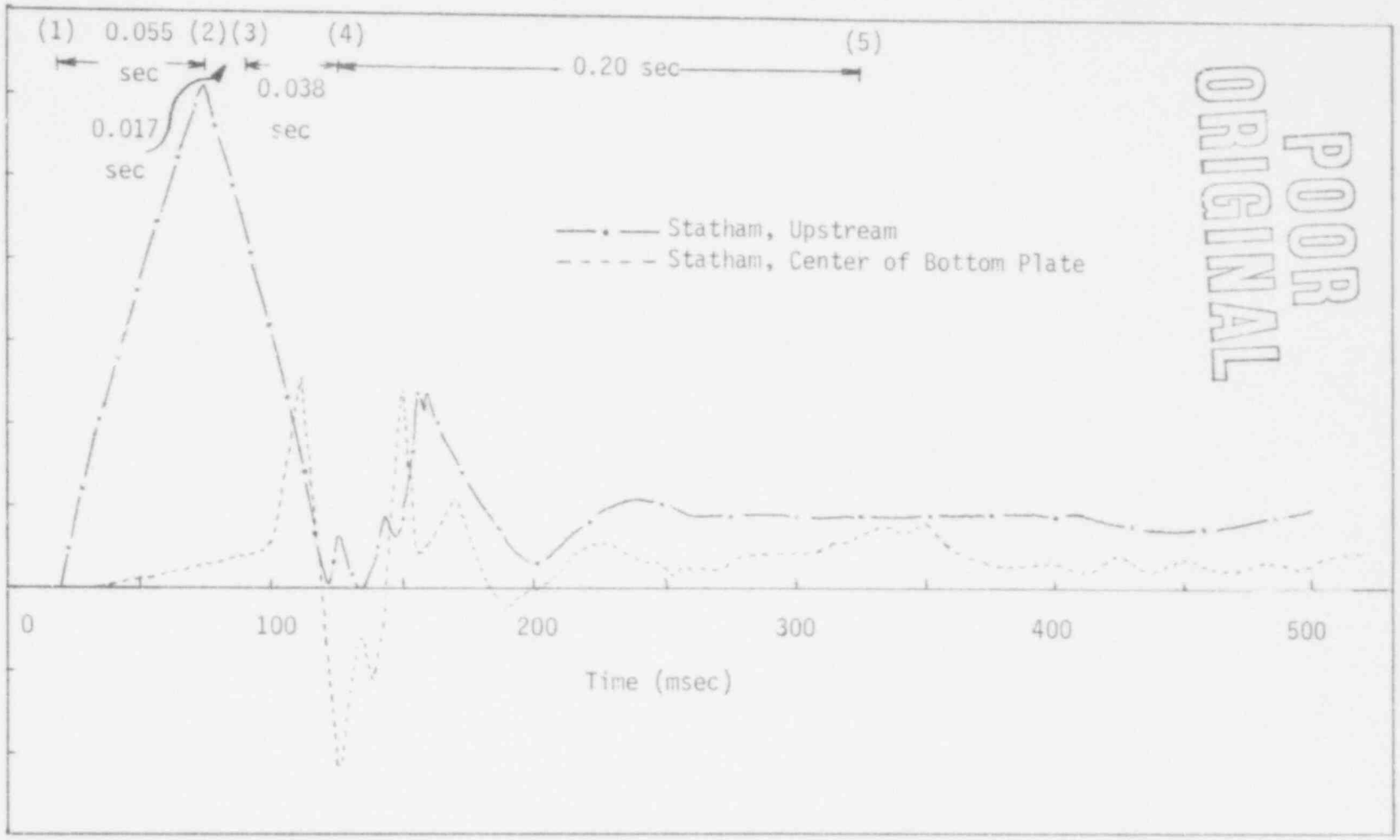

Figure 3.21. Pressure Forces Generated on the Upstream and the Bottom Plate during Vent Clearing (4.6 cm ID Tube) with Upstream Pressure of 135.8 kPa.

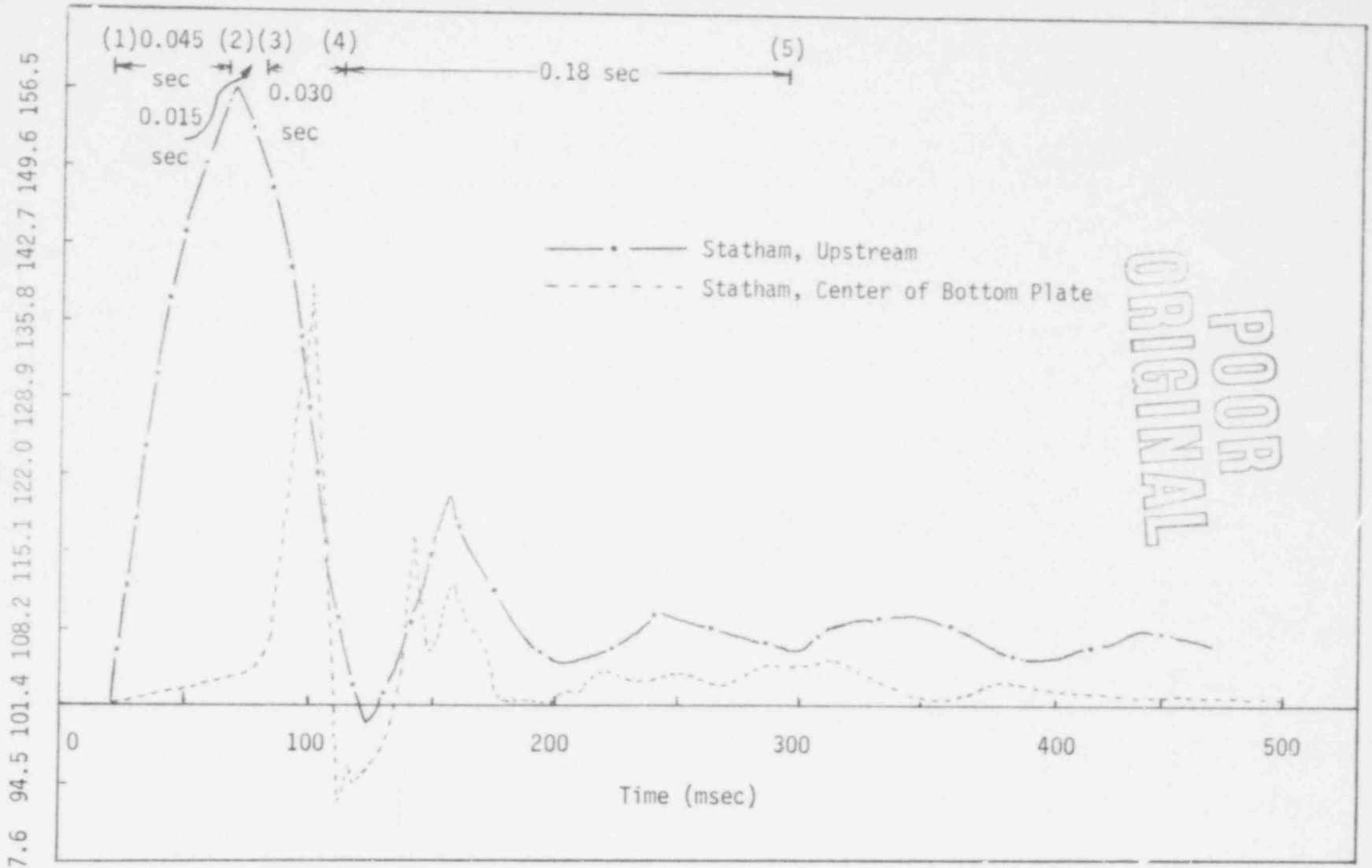

Figure 3.22. Pressure Forces Generated on the Upstream and the Bottom Plate during Vent Clearing (4.6 cm ID Tube) with Upstream Pressure of 149.6 kPa.

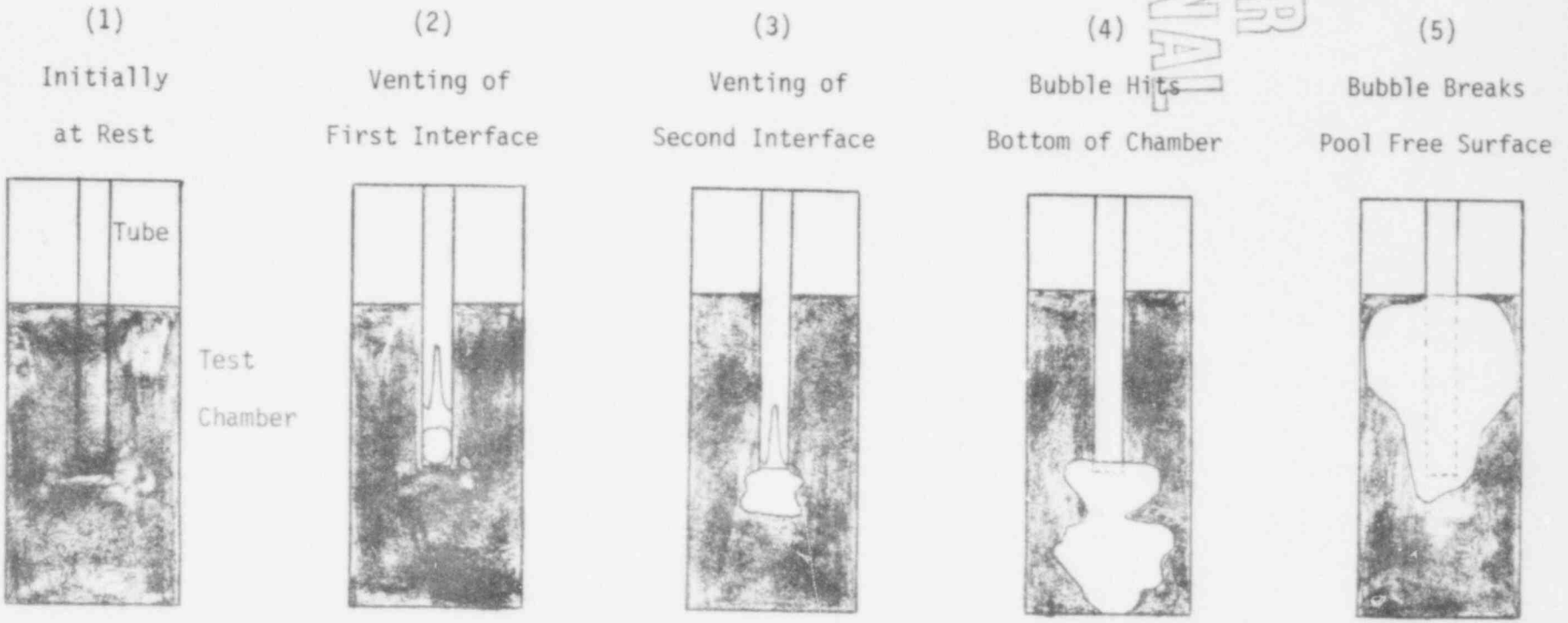

Figure 3.23. Illustration of the Various Stages of Vent-Clearing and Bubble Growth Phenomena. (The Numbers Correspond to Those Denoted in Figures 3.20, 3.21 and 3.22.)

the steam is not considered at this stage but will be considered at a later stage.

The initial equipment set-up includes a hexagonal aluminum observation tank, steam supply (100 psig max., saturated or superheated steam up to 1 lb/min), water supplies, and instrumentation for monitoring temperatures, pressure and flow rates of steam, as shown in Figure 3.24.

The basic criteria adopted in this design are as follows:

(a) leak-proof system,

(b) pure and clean system supply with no uncontrolled air content or other contamination,

(c) degassed water pool, and

(d) sturdy test chamber with transparent windows for visual observations.

The coolant loop consists of four major components, namely, a boiler, a superheater, a storage tank and a feed pump. The saturated steam generated in the boiler is superheated in the superheater. It is then stored for steam injection which is initiated by an electrically activated valve, V2. This valve controls the rate of steam injection into the pool. Condensation is expected to occur in the pool water and by opening valve V4 the condensate is then fed back into the boiler.

The system is started up by turning on the heaters H1, H2 and H3 (Fig. 3.24). Valves V3 and V5 are opened while V2 and V4 are closed after that part of the line is filled with steam. The air initially in the system is then driven out through V5 and V3 by the steam generated in the boiler. At the same time the water is also degassed since the solubility of air decreases as the water temperature rises. The time period necessary for this process is tentatively taken to be approximately one

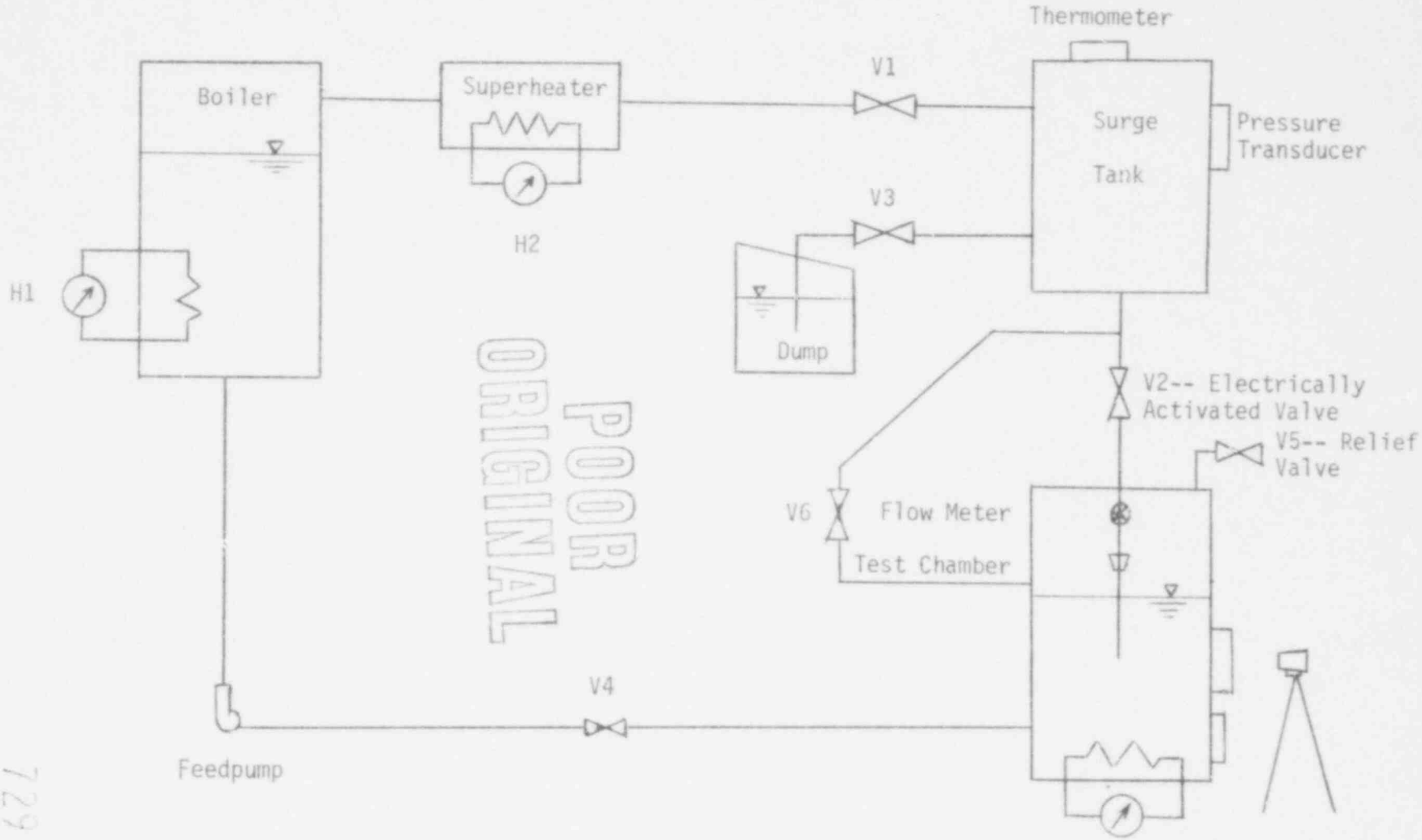

Figure 3.24.

Schematic of Preliminary Design for Steam Injection Experiments.

hour. After the start-up stage valve V3 will be closed and V4 will be opened. A certain time period is also required to build up the system pressure after valve V3 is closed. The experiment can be started after the system has achieved the required pressure. The experiment is started by electrically activating valve V2 to allow steam injection into the pool.

3.4.2. Design Basis of Each Component in the System

1. Boiler-- the boiler is designed to have a heat load of 17 kW and to operate at a pressure of 100 psig, generating steam at approximately one pound per minute.
2. Superheater-- the superheater is designed to dry the saturated steam and may be used to superheat the steam slightly. The designed maximum heat load for the superheater is 1.5 kW and it is variable.
3. Feed Pump-- the flow rate versus pressure difference across the pump will be studied and calibrated. The operating condition of the pump is designed to feed water into the boiler at 100 psig at the rate of one pound per minute.
4. Test Chamber-- the pool is designed to be 18 inches in equivalent diameter and four feet in height. Heater H3 is uniformly distributed at the bottom of the pool. The maximum power of the heater H3 is 1.5 kW. Two six inch diameter glass window openings are designed. The top opening is centered at the end of the injection pipe. The bottom opening is 1.0 foot below the top, such that light can shine on the steam jet at a 45 degree angle. The camera will be located at the front window.

7. Miscellaneous-- five stainless steel gate valves all sized two inches are required for system control. Pressure transducers capable of measuring transient pressures for steam and for the pool water are still under investigation. The flow meter to measure the transient flow of steam at the injection pipe is to be tested and calibrated.

In summary, the general design concept is worked out. Details of each component still require further study before the experiment can be started. The major components that will require extensive study are the flow meter, the pressure transducers, and also the techniques for transient temperature measurement.

729 112

APPENDIX A -- PHOTO-TECHNIQUE

During the second quarter, extensive effort has been spent on the improvement of the photo-technique for a better movie recording of the interfacial motion. The governor and gearing system on the Photosonics 1B-AC nigh speed movie camera have been modified to give a constant 680 frames per second (fps) at full speed. A method of remotely controlling the starting of the camera has also been developed.

A 135 mm telephoto lens has been fitted to the Photosonic camera to allow focusing on a much smaller field of approximately four inches. Formerly a 13 mm wide-angle lens was used that limited the field size to approximately one foot. The use of the telephoto lens also increases the depth of field for better resolution of the three dimensional bubble surfaces.

An improved through-the-lens viewing system has been adapted to the Photosonic camera to allow more precise focusing. Improved focus has allowed better resolution at exposure times of 1/3,400 second. Because this Photosonic camera has an adjustable rotating shutter as well as a rotating prism, exposures of up to 1/27,200 second are possible, but lighting intensity becomes critical at these short exposures.

Three thousand volts of tungsten filament lighting is used for exposures of 1/3,400 second. The lighting is remotely controlled and turned on for only brief periods of time to prevent melting of the plexiglass cylinder. Expertise has been developed in the use of a light meter with an extrapolated exposure time scale that permits exact camera aperture settings in this high intensity lighting situation.

Kodak Tri-X reversal film with an ASA rating of 160 has been used effectively with exposures of 1/3,400 second. In the future as work is

done with decreased exposure times, 4-X reversal film with an ASA rating of 320 will be used and eventually 4-X negative film pushed to ASA 1,000.

Editing and processing experience has been gained. A 16 mm Bell and Howell movie camera with a speed of 18 fps has been used for titling and parallax correction data has been compiled. Composite printing of a white grid over footage of a growing bubble has been performed by a film processing laboratory in West Hollywood.

A new system for putting timing flashes on the film has been developed. More intense flashes of greater frequency are needed as the filming speed increases. The flashes have been synchronized to start when the upstream air system valve is activated.

Film breakage at high speeds has been encountered, but precise adjustment of the film take-up clutch has minimized this problem. Excessive camera and lens vibration has also been encountered and minimized by clamps and supports.

Experience is presently being gained in the use of a Kodak 3,000 fps camera. A camera capable of 5,000 fps is on order through the Oak Ridge excess property listings.

APPENDIX B -- PRESSURE TRANSDUCER CALIBRATION

Various pressure transducers were tested to determine their time responses to dynamical pressure. First, a Celesco LC-10 hydrophone was tested. In accordance with the specifications, a free field frequency response of 2.78 μV/μb for a frequency range from 0 to 300 kHz was obtained. The capacitance across the leads was 7,146 pf and the resistance was 100 kΩ. The capacitance was checked using a simple electric circuit. The hydrophone was mounted as shown in Figure B.1 at the end of a seven inch tube extended from a solenoid valve. The output of the hydrophone is summarized in Table B.1. A typical response of the hydrophone analog output is shown in Figure B.2. The response time is about 4 msec. As shown in Table B.1, the voltage observed in the test is different from the calibration by a factor of two. This is probably due to the slow transient time which is not the original design of the hydrophone.

In place of the hydrophone, the procedure was repeated with a Celesco KP15 variable reluctance pressure transducer in conjunction with a model CD-25 transducer indicator. According to the vendor, the time response is less than 1 msec. The results of the tests show that the rise time of the Celesco transducer is 120 to 140 msec, for a quick release of upstream pressure (3 to 6 psig). A typical oscillogram is as shown in Figure B.3. The time response characteristic of the Celesco is therefore unsatisfactory.

The Statham differential pressure transducer model PM 131TC is an unbonded, fully active strain gage type transducer (±15 psig). The response time, which is 1/5 of the natural frequency, is estimated to be 0.6 msec based on information supplied by the vendor. The output of this

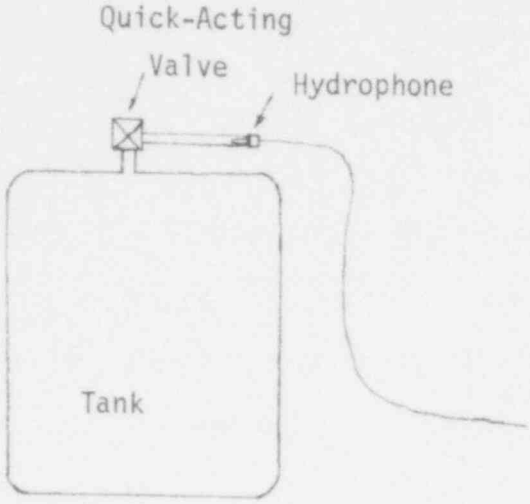

Figure B.1. Experimental Setup for Calibrating Hydrophone (Celesco LC10).

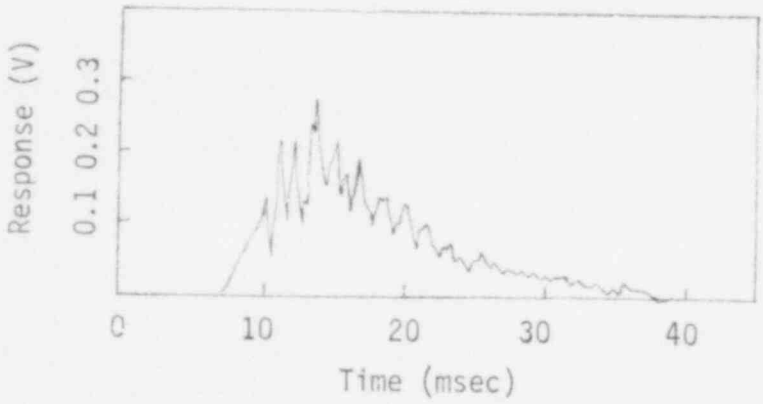

Figure B.2. Typical Analog Response. The Upstream Pressure Was 3 psig.

Tank Pressure (psig)	Observed Voltage (V)	Calculated Voltage (V)
2	0.15	0.378
3	0.30	0.567
4	0.34	0.756
5	0.34	0.945
6	0.42	1.13
7	0.45	1.32

Table B.1.

Calibration Table of Hydrophone LC-10.

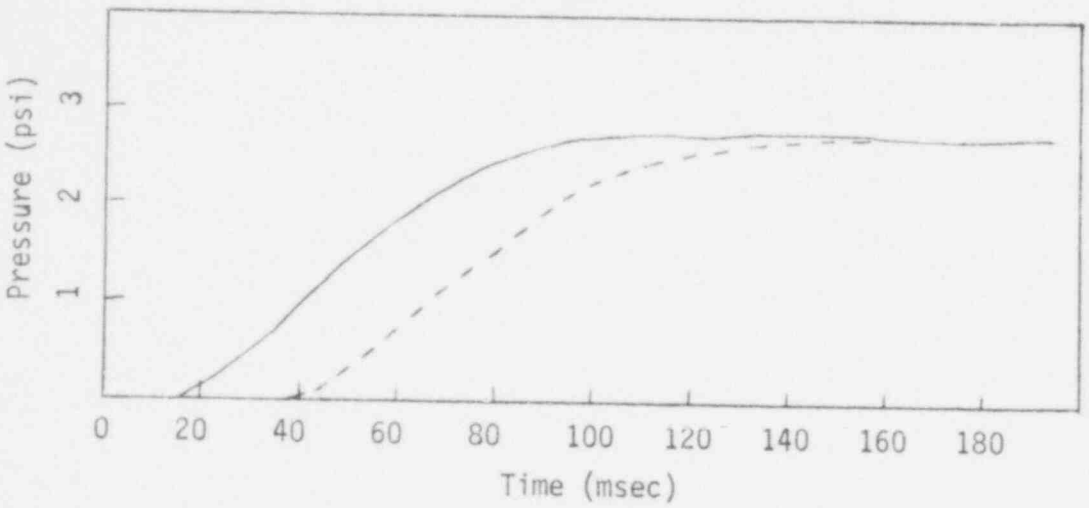

Figure B.3. Time Response of Celesco KP15 Pressure Transducer to a Release of 3 psig Upstream Pressure through a Solenoid Valve. The Full and Dotted Lines Are the Transducer Output with the Valve Located 5" and 12.5' Away, Respectively.

transducer is nominally 4 mV/V corresponding to a full scale output of 20 mV for 15 psid. A 5 V excitation is required. A static test was first performed and the result is shown in Figure B.4. The fluctuation in the calibration curve appears to be due to difficulty in eliminating the noise from the transducer analog output since the transducer is operated in a low level range.

The Statham transducer was tested against the Celesco transducer by detecting the pressure of a rapidly opening valve, and the results are shown in Figure B.5. The rise times are summarized in Table B.2. It is observed that the Statham transducer has a far quicker response than the Celesco unit. The only drawback to the Statham product appears to be its small analog output (20 mV full scale). Pre-amplification of the signal would be required for the use of this transducer with the mini-computer being purchased at this time. An Endevco 4621A DC amplifier was recently used in conjunction with the Statham transducer. We were able to magnify the transducer output one hundredfold, but a time delay of about 200% was also noted. The Statham has the added advantage of being capable of flush-mounting on the bottom plate of our test chamber. This helps to eliminate the sprung-mass damping effect found in most cavity type arrangements (the water mass in the cavity being significant with respect to the mass of the sensing element of the transducer). Also, we can eliminate the errors incurred with a sloppily made cavity, since it is know that a cavity with a rough, burred finish can result in as much as 5% error by itself.

729 119

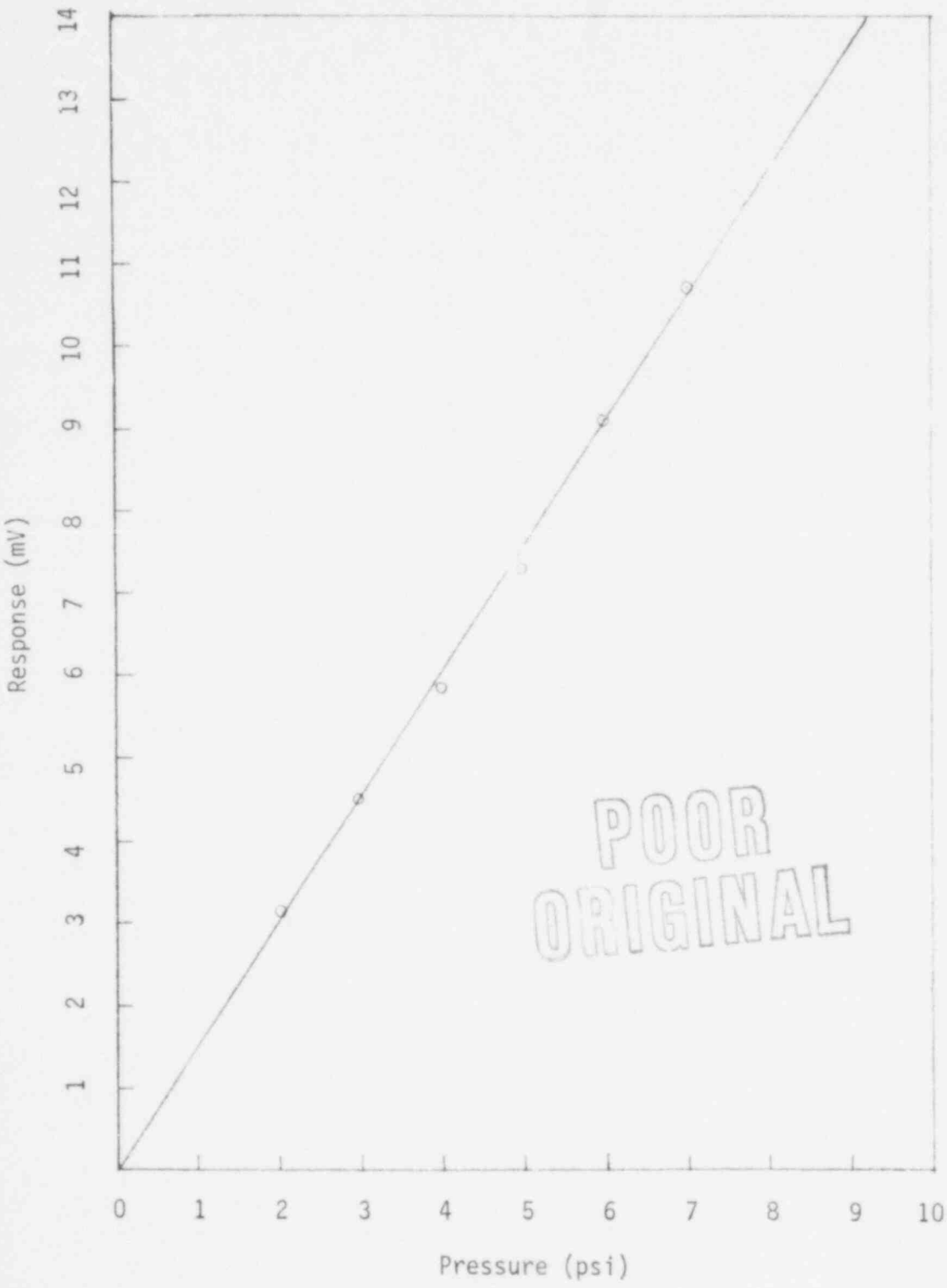

Figure B.4. Static Calibration of Statham PM 131TC Pressure Transducer.

127 120

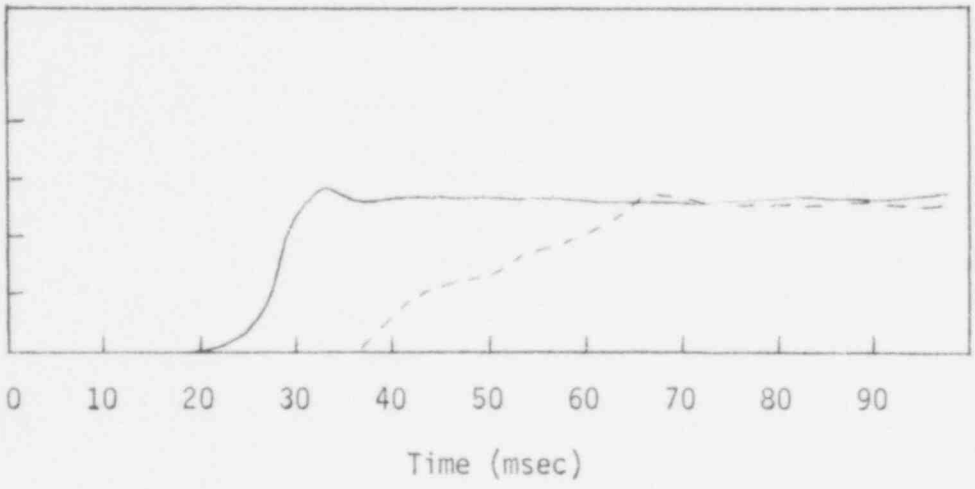

Figure B.5. Time Response of Statham PM 131TC Pressure Transducer to a Release of 3 psig Upstream Pressure through a Solenoid Valve. The Full and Dotted Lines Are the Output with the Transducer Located 5" and 12.5' away from the Valve Respectively.

	Pressure (psig)	Rise Time (msec)
Statham	3	8.0
	5	7.5
	7	6.5
Celesco	3	130
	5	120
	7	130

Table B.2.

Response of Statham and Celesco Transducers

to Pressure Upstream through a Solenoid Valve.

APPENDIX C -- CALIBRATION OF THE AIR FLOW METER

A transient calibration of the TSI Model 4100 air flow meter was carried out by noting the flow rate during empying of an air reservoir of unknown volume. The total pressure in the reservoir was also recorded as a function of time. Knowing the time variation of the chamber pressure, Bernoulli's equation was solved for the flow rate as a function of time. Figure C.1. shows the flow rate as given in analog output of the flowmeter and the predicted flow rate when the coefficient of discharge is assumed to be 0.65. For all three upstream pressures, the transient response of the flowmeter is seen to be in good agreement with the predictions. Because the maximum operational capability of the 4100 flowmeter is 70 m/sec, no data could be obtained when the actual flow rate was greater than this value.

A typical flowmeter response during vent clearing is shown in Figure C.2.

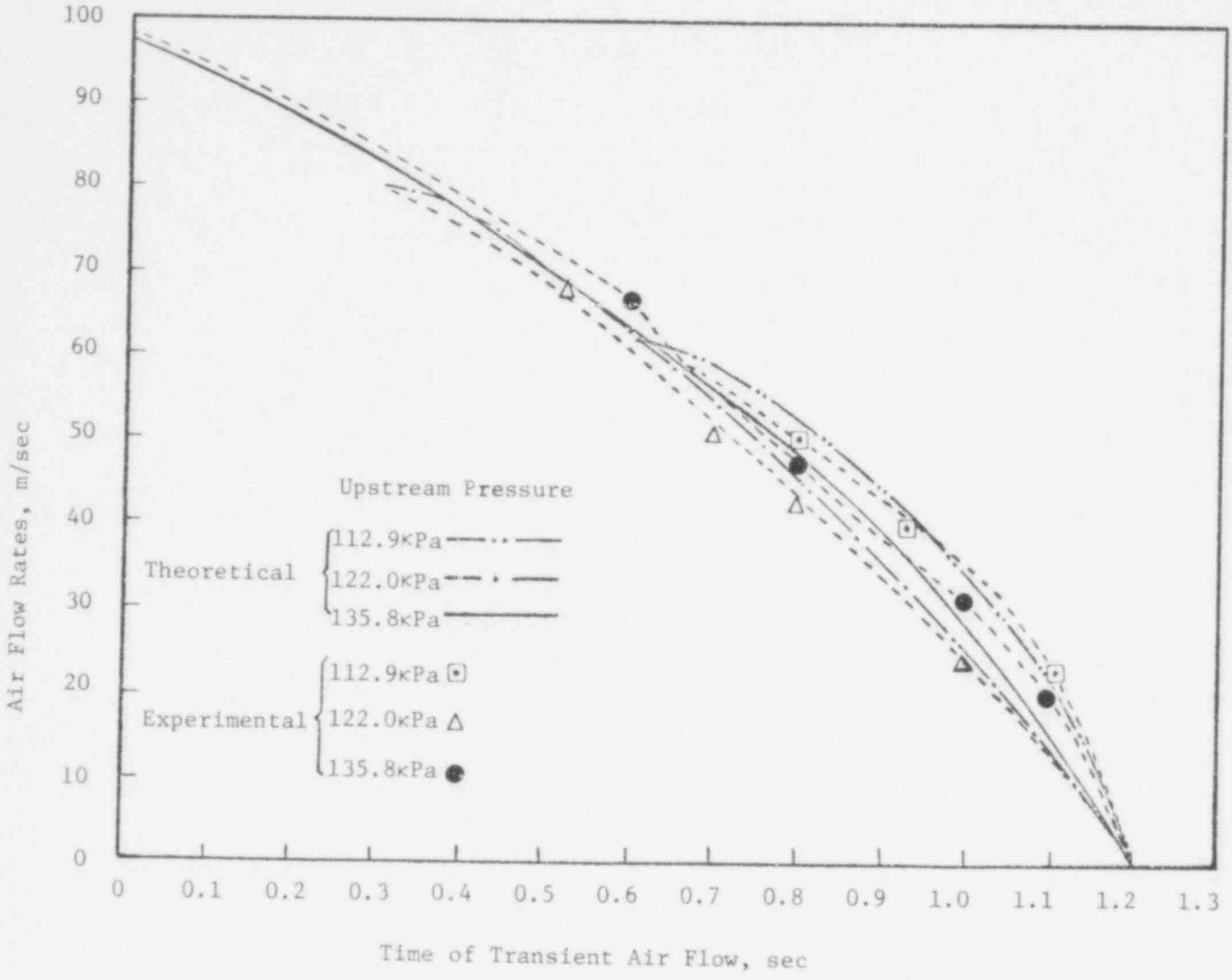

Fig. C.1. Comparison of Flow Rates Calculated Theoretically and Monitored by the Model 4100 Airflow Meter during Transient Air Flow Tests.

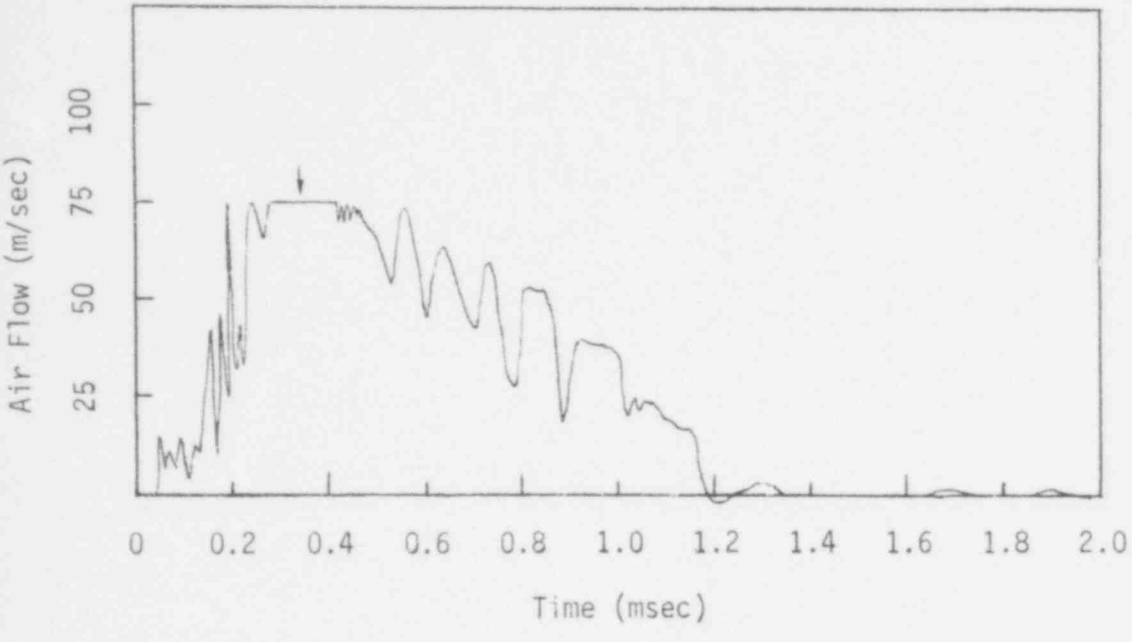

Figure C.2.

The Time Response of the TSI 4100 Air Flow Meter. The Flat Plateau (Marked by an Arrow) Indicates the Limit of Operational Capability. Upstream Pressure is 4 psig.

729 125

UNITED STATE
NUCLEAR REGULATORY OMMISSION
WASHINGTON, D. C 20555

OFFICIAL BUS NESS
PENALTY FOR PRIV E USE, $300

POSTAGE AND FEES PAID
UNITED STATES NUCLEAR
REGULATORY COMMISSION

U.S.MAIL